Title
Mechanical and Opto-mechanical Properties of Branched Semiconductor Nanocrystal Stress Sensors

Author
Raja, Shilpa Naresh

Publication Date
2016

Peer reviewed|Thesis/dissertation

Mechanical and Opto-mechanical Properties of Branched Semiconductor Nanocrystal Stress Sensors

By

Shilpa Naresh Raja

A dissertation submitted in partial satisfaction of the
requirements for the degree of
Doctor of Philosophy
in
Engineering-Materials Science and Engineering
in the
Graduate Division
of the
University of California, Berkeley

Committee in charge:
Professor A. Paul Alivisatos, Chair
Professor Robert O. Ritchie
Professor Liwei Lin

Summer 2016

Abstract

Mechanical and Opto-mechanical Properties of Branched

Semiconductor Nanocrystal Stress Sensors

by

Shilpa Naresh Raja

Doctor of Philosophy in Materials Science and Engineering

University of California, Berkeley

Professor A. Paul Alivisatos, Chair

This dissertation highlights advances in using semiconductor tetrapod quantum dots (tQDs) as stress sensors in structural polymer nanocomposites. Semiconductor nanocrystals have undergone many developments in terms of synthetic control of shape and size since their inception, and one example is the ability to create branched nanocrystals such as tQDs. tQDs are core/shell tetrahedrally symmetric, branched nanocrystals. In this thesis, studies will utilize tQDs consisting of a ~4 nm cadmium selenide (CdSe) core and ~25 nm long cadmium sulfide (CdS) arms. Their type I band alignment and the modulus difference between their core and shell, along with their branching, makes them sensitive to applied mechanical environmental stresses. The CdS arms receive stress from a host matrix in which the tQDs are embedded and transmit it to the CdSe core. The tQD's photoluminescence emission spectral maximum undergoes a monotonic red-shift, or decrease in energy, with increasing tensile stress, due to widening bond distances in the core. The tQD's property of nanoscale stress-sensing is of relevance to fields such as polymer dynamics, sensing of premature fracture in service, and biomechanical stress sensing.

We have fabricated and characterized the structure and opto-mechanical sensing ability of a wide variety of tQD-polymer nanocomposites. We demonstrate tQD sensing of tension and compression as well as more complex stress responses, such as stress relaxation and hysteresis. We perform optical and mechanical tests simultaneously, discovering a new sensing modality, and orders of magnitude of stress amplification in the tQD core. We also discover tQD sensing of dispersion including a switch in optomechanical response characteristic when tQDs are in direct contact.

In addition to demonstrating and analyzing these new phenomena, we theoretically explore, with micromechanical finite element simulations and atomistic density functional theory, the origins of the tQD stress response. We further examine, experimentally and theoretically, the ability of tQDs to serve as mechanical fillers, finding that they have greater potential to improve the Young's modulus of structural polymers than linear nanorods and nano-spheres due to their branched shape. The results in this dissertation contribute to the understanding of the structural, mechanical, and optical sensing properties of nanocomposites of polymers and semiconductor tQD nanocrystals.

Acknowledgements

Thanks to my family, friends, and mentors in-and-out of the workplace whose support and light-heartedness made my graduate studies enjoyable.

Thanks especially to Siva Wu, Andrew Luong, Alex Powers, Nick Borys, Matthew Koc, Andrew Olson, Lindsey Hanson, and Danylo Zherebetskyy for their time.

Thanks to Profs. Alivisatos, Ritchie, Lin, Asta, Xu, Govindjee, and Gronsky for their time, mentorship and guidance.

Table of Contents

List of Figures

List of Tables

Chapter 1 : Introduction

1.1: Motivation

Polymer-nanoparticle composites can exhibit enhanced mechanical properties and unique functionalities[1-7], enabling new functional materials such as antimicrobial polymers[8] and biocompatible implants[9]. However, rational design of these materials has remained elusive, due to a lack of detailed understanding of stress profiles at the microscale and nanoscale. Specifically, an understanding of the interface between the filler and polymer and how stresses are transferred across that barrier are critical in reproducibly synthesizing composites[10-13].

Furthermore, as premature failure of structural components invariably results from the initiation and incipient growth of small cracks,[14-16] there is a vital need for auto-responsive structural materials that potentially self-detect and self-respond to environmentally-induced mechanical damage[17]. Such materials have a built-in potential to prevent catastrophic failure in service applications[18]. However, current technologies that can provide for the early self-detection of local stresses associated with stresses at the polymer-nanoparticle interface or incipient cracks are extremely limited[19,20].

Established techniques for these studies—including micro-Raman spectroscopy[21], synchrotron radiation[22], and electron backscattering[23] as well as contact techniques such as atomic force microscopy[24,25], nanoindentation[26], and others[27]—are difficult to adapt to *in vivo* stress detection and premature failure detection in service due to their stringent requirements in sample size and shape or need for controlled laboratory environments[20]. Recent advances in smart materials have used self-reporting fillers such as near-infrared molecular probes[28], micron-sized ZnO tetrapods[29], metal nanoparticles[30,31] and bio-inspired concentric optical fibers with varying refractive index[19]. However, these fillers have drawbacks, including altering the molecular-level composition and structure of the polymer and weakening multiple mechanical properties such as toughness[29]. Mechanophoric dyes and piezoresistive materials, for example, are only effective at the millimeter length-scale with relatively low sensitivity;[30,32-34] furthermore, such techniques are also very challenging to implement "in the field".[14,19,20,29,30,32-37]It is therefore of considerable interest to develop an optical luminescent stress sensing nanoparticle, and to establish ways of embedding these inside polymers without perturbing the mechanical properties that are being sensed. Such a visible-light, nanoscale sensor with the ability to be embedded into a variety of "smart" structural materials without causing such degradation would be particularly appealing for the potential sensing of impending fractures in service.[18] Furthermore, mechanical stresses exerted by biological tissues can be signatures of disease[38]. Thus, such a sensor, if embedded into soft polymers[39,40], could also potentially be of significant use in biological applications such as sensing of stresses in cancer cell proliferation[20,41].

Colloidal semiconductor quantum dots display a multitude of size and shape-dependent properties, enabling their use in a variety of electronic and optical applications[42]. The ability to tune their size and shape, and in particular the ability to create branched nano-heterostructures,

provide further opportunities to take advantage of their special behaviors[43]. One such opportunity is the creation of functional nanocomposites with specific "smart" characteristics, such as shape-dependent mechanical properties or self-healing properties upon exposure to radiation[11,44,45]. The cadmium selenide-cadmium sulfide (CdSe-CdS) core/shell tetrapod quantum dot (tQD) is a particularly interesting system. The tQD is a branched, tetrahedrally symmetric colloidal semiconductor nanocrystal consisting of a zinc-blende CdSe core and four epitaxially grown wurtzite CdS arms[46]. To improve synthetic yield[47], tQD cores are synthesized separately in the presence of oleic acid and oleylamine, followed by shell growth in the presence of octadecylphosphonic acid, resulting in native hydrophobic alkyl chain ligand coverage[46,48,49]. These quasi-type I heterostructures are highly emissive with large extinction coefficients and high quantum yields in the visible range[49,50]. Due to the tQD's branched morphology, in which the four long CdS arms confer a net stress on the CdSe core upon deformation, the tQD exhibits a photoluminescence stress response[51]. In response to nano-Newton forces, they were predicted to have a monotonically decreasing band-gap[51,52]. The potential for tQDs to be useful as a stress sensor[49,50,53] was recognized early on with studies that showed the tQD's monotonic photoluminescence emission maximum redshift in response to tensile stress in diamond anvil cells[54] (Fig. 1.1), under atomic force microscope (AFM) tips[52] and in semi-crystalline polymers[18,20]. These studies opened the way for further investigations as shown in this thesis, which extended the early work[20] by utilizing simultaneous or side-by-side mechanical testing, processing methods such as electrospinning or film casting which allowed for tunable tQD dispersion and concentrations in the composite[18,20,55], and by studying sensing in structural films rather than fibers[18,20,55]. Owing to its nanoscale size and branched shape[54], the tQD provides a far higher spatial resolution of stresses than existing technologies[20,56].

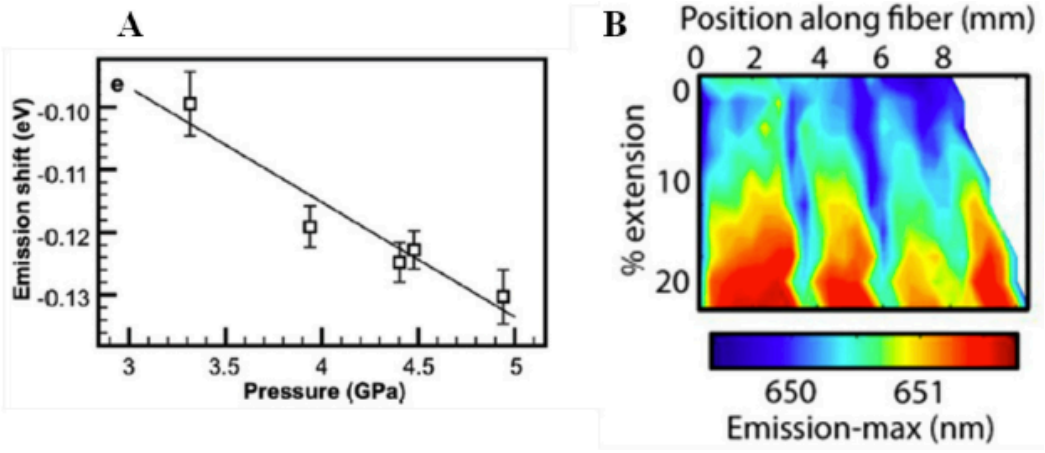

Figure 1.1: Previous studies on tQD stress response
(A) tQDs exhibited a linear response to increasing pressure when embedded into a diamond anvil cell. (B) A stress map of the fluorescence redshift of tQDs with increasing strain along the fiber axis in tQD-fiber nanocomposites prepared via diffusion. Figure adapted from references 20 and 49.

Herein, we demonstrate that it is possible to use luminescent semiconductor nanocrystal tQDs as stress sensors in multiple formats that build on previous works, deepening the understanding of tQD stress-sensing mechanisms and using a variety of different processing

techniques to demonstrate their potential for stress-sensing in service. We incorporate tQDs into polymer fibers via electrospinning, allowing for much larger, variable concentrations than previous works, and perform side-by-side mechanical tests to compare tQD optical and mechanical responses. We find that tQDs can be incorporated into electrospun fibers at high concentrations without changing the inherent mechanical behavior of the fibers. We also incorporate tQDs into films of hydrophobic polymers with which they interface relatively well, and conduct simultaneous optical and mechanical tests which reveal an excellent level of opto-mechanical agreement in films as compared to fibers. We show the ability of tQDs to sense when they are in direct contact, and discover a new sensing modality, the sensing of stress in terms of the full-width half maximum; previous tQD stress sensing was limited to red-shifts of the photoluminescence emission maximum. tQDs uniquely report the stress state of the nanofiller phase; we show, via density functional theory calculations and finite element calculations, that at high packing densities tQDs detect stress via photoluminescence blue-shifts rather than red-shifts because of net compression in the nanofiller phase. We further show that in softer polymers, tQDs can exhibit a pressure coefficient orders of magnitude higher due to the unique stress amplification effects of the tQD.

In addition, we explore the ability of the tQD to tune the elastic modulus of structural rubbers and compare their performance as a mechanical filler to nanorods and spherical quantum dots. Studies in this regard were conducted over a variety of concentrations in electrospun fibers and films, and lattice spring model simulations of the nanocomposites were employed to explain the results. We find that due to their branched shape, which optimizes both the orientation of strong X-type interfacial bonds and filler bonds with the tensile axis, tQDs provide the best enhancements of nanocomposite Young's modulus[44].

1.2: Dissertation Organization and Flow

The general structure of this dissertation involves building upon previous work by first engaging in studies of tQDs as sensors in electrospun fiber nanocomposites (Chapter 2) and then progressing to studies in structural films (Chapter 3) followed by a study of the effect of nanocrystal branching on the nanocomposite Young's modulus (Chapter 4).

We start in Chapter 2 with electrospun fiber composites in order to potentially achieve better dispersion using high electric fields, and because electrospun fibers provide a simple model system with facile, efficient fabrication in which many samples can be quickly and reproducibly prepared for side-by-side optical and mechanical tests. With electrospinning, dozens of samples can be prepared from one drop of precursor solution. It was important to have Chapter 2 demonstrates, using side-by-side optical and mechanical tests, the capacity of tQDs to serve as a non-perturbing probe in hydrophilic polyesters, i.e., a self-embedded nanocrystal filler that senses the stresses in the nanocomposite without degrading its mechanical properties. Because films have more structural applications than fibers, e.g. as stress-reporting adhesives or coatings, we next in Chapter 3 expand on fiber studies by studying tQD stress-sensing in thick films of structural rubbers, uncovering more complex stress responses and orders of magnitude higher stress sensitivity in structural films. In contrast to the results in Chapter 2, Chapter 3

shows that in hydrophobic structural rubber films, tQDs can enhance the elastic modulus of the composite under certain processing conditions. This may be useful for specific applications that require a range of tunable nanocomposite Young's moduli in addition to a built-in stress-sensing ability. We therefore end in Chapter 4 with a study of the effect of nanocrystal branching and tQD concentration on nanocomposite Young's modulus in structural hydrophobic fibers and films.

Brief summaries of each chapter follow.

Chapter 2 will describe the use of tQDs as stress sensors in electrospun fibers, revealing sensing of new more complex behaviors such as stress relaxation and hysteresis, as well as demonstrating the tQD as a non-perturbing probe.

Chapter 3 will describe the use of tQDs as stress sensors in nanocomposite films, revealing a packing density-dependent sensing of both tension and compression in the filler phase, a new sensing modality, and stress amplification in soft hydrophobic polymers.

Chapter 4 will describe the use of tQDs as optimal nanoscale fillers (as compared to spherical quantum dots and linear nanorods) to enhance the elastic modulus of nanocomposites.

Chapter 5 provides a brief outlook on future research directions.

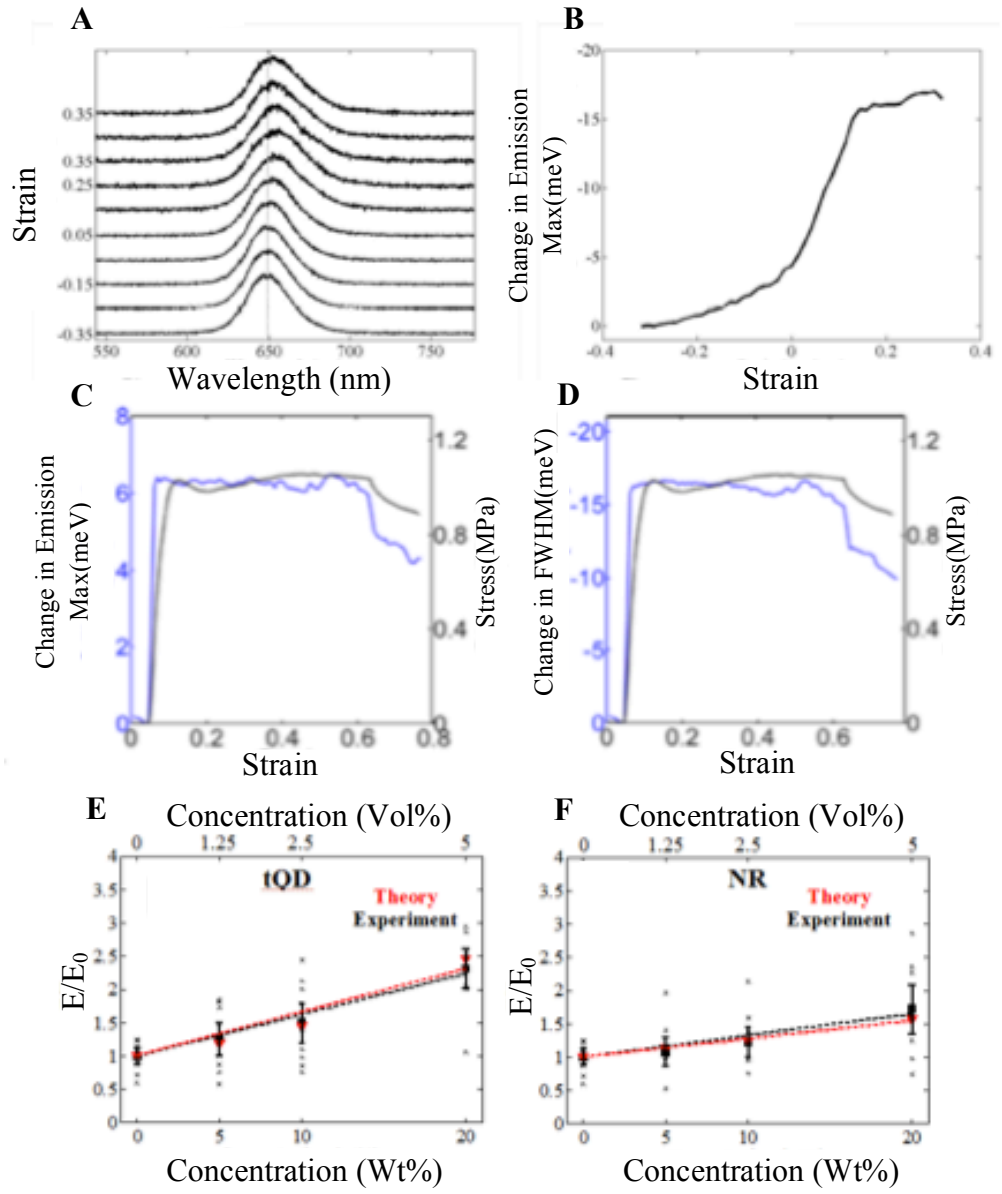

Figure 1.2: Overview of advances in this dissertation
(A-B) tQDs exhibited a response to applied stress in electrospun fibers that matched features of traditional uniaxial tensile curves, such as slack, an initial linear elastic regime, and a regime of plastic deformation. (C-D) Results of opto-mechanical stress testing on tQD-polymer nanocomposite films, indicating close agreement of the tQD-sensed fluorescence tensile curve with the one measured by a traditional bulk load cell, including sensing of stress relaxation. (E-F) Results of mechanical tests and simulations on tQD and nanorod-polymer composites, indicating the superior performance of the tQD as a mechanical filler.

Chapter 2 : tQDs as Fluorescent Stress Probes of Electrospun Nanocomposites

2.1: Introduction

Rational design of composites with optimized mechanical properties requires understanding of how stresses are transferred across the interface between the filler and polymer. However, there is a lack of detailed quantification of stress profiles at both the microscale and nanoscale to correlate the local stress with polymer-filler interaction, polymer chain conformation and dynamics. [10,57] Established techniques such as micro-Raman spectroscopy[21], synchrotron radiation[22,37], electron backscattering[20], AFM[10] and nanoindentation[58], etc.[59] are difficult to adapt to *in situ* and premature failure detection in service due to sample requirements or need for controlled laboratory environments. Recent advances in smart materials have used self-reporting fillers such as near-IR molecular probes[28], micron-sized ZnO tetrapods[29], metal nanoparticles[30,31] and bio-inspired concentric optical fibers with varying refractive index[19]. However, these fillers are in general microscopic in size, making them unsuitable for nanocomposites, or degrade the mechanical properties of the host material. tQDs have significant potential as stress sensors[54]. With a zinc-blende CdSe core and four tetrahedrally branched wurtzite CdS arms, these nanoheterostructures are highly emissive in the visible range[49]. In response to nano-Newton forces, they were predicted to have a monotonically decreasing band-gap[51,52] and were shown to have a fluorescence red shift in response to non-hydrostatic gigapascal stresses[54].

The surface chemistry of tQDs can be easily modified following established nanoparticle ligand exchange[60], which can allow them to be easily incorporated into a wide number of synthetic and biological polymers with variable concentration and dispersion. Despite this, previous studies featured only very dilute (~0.002% by weight) incorporation of these nanocrystals into polymers via diffusion[20].

In this chapter, we substantially extend the range of loading by employing electrospinning as a means of introducing the tQDs into the polymer. Electrospinning involves the application of a high electric field to a droplet of viscous polymer solution, resulting in the formation of a taylor cone[59] that splays into a network of fibers at the metallic collector[61,62]. We chose electrospinning for two main reasons. The first is that we hoped that the high electric fields used, >=15 kV/cm[18], would result in good dispersion of the tQDs in the fiber. The second was that it is allows for the creation of dozens of fiber samples of uniform thickness and length from simply a few microliters of precursor solution[18]. This was an attractive prospect because tQDs can be challenging to prepare in high yield. A facile, quick means to prepare many samples from a small quantity of tQDs, to get significant statistical data on the tQD opto-mechanical response, was appealing for an initial work aimed at improving understanding of tQD stress-sensing mechanisms. We incorporated, via electrospinning, several concentrations of tQDs (from 3.6-40% by weight) into poly-l-lactic acid (PLLA), forming a nanocomposite material with PLLA as the polymer matrix host material, and the tQD as the nanoscale composite filler material. PLLA was chosen for our initial study because its electrospinning fabrication process is especially

robust and well-developed[63,64]. Optical and mechanical experiments on this nanocomposite show that the tetrapod nanocrystal sensor matches the bulk mechanical sensor with a reasonable degree of agreement in the basic tensile mechanical properties as well as under cyclic loading and stress relaxation**.** Several differences between the sensing behavior of the universal testing machine (UTM) macroscale load cell and the tQD nanoscale load cell are observed, which we attribute to an imperfect polymer-nanocrystal interface and consequent incomplete stress transfer to the tQD filler[10]. As discussed below, particle aggregation during composite formation limits stress transfer to the tetrapods, which ensures elasticity and recyclability of the probe by preventing plastic deformation of the non-perturbing (i.e., causes no change to the mechanical properties) nanoscale sensor. We further show that increasing the tetrapod concentration, while affording little to no change in the polymer mechanical and structural properties, effectively improves the tQD sensor response and sensitivity. Finally, we examine the stress relaxation and cyclic deformation/hysteresis of the polymer composites using the tQD deformation sensor. The most important results of this chapter are the presentation of optical and mechanical tests conducted side-by-side for the first time, which helps to advance the understanding the performance of tQDs as stress sensors and reveal new sensing responses.

2.2: Nanocomposite Electrospinning

In order to incorporate tQDs into poly-l-lactide (PLLA) polymer at a large range of concentrations to investigate the impact on mechanical properties as well as the opto-mechanical self-sensing ability of the polymer nanocomposite, we used electrospinning, a versatile technique for micro- and nanofiber formation, which involves applying a large electric field (approximately one kilovolt/centimeter or higher) to a droplet of polymer solution on the end of a syringe needle[65]. Upon sufficiently high electric field application, the droplet loses its spherical shape and begins to elongate, forming a shape termed the Taylor cone[59]. Subsequently, a jet stream erupts from the unstable Taylor cone, forming fibers at the grounded electrode (Fig. 2.1)[66]. The large electric field may cause nanocrystals and particle aggregates to be more uniformly dispersed throughout the polymer matrix than other nanocomposite fabrication methods[67,68]. This may minimize the formation of stress concentrations within the nano/microstructure, which would act to degrade the mechanical properties of composite materials[69,70].

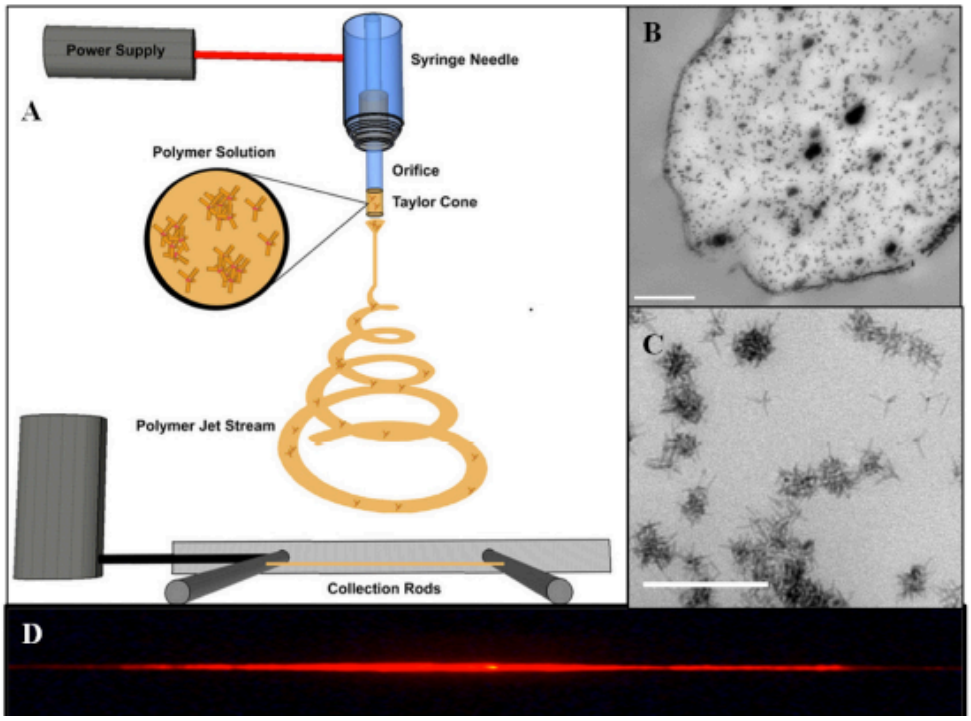

Figure 2.1: tQD-PLLA composite electrospun fibers
(A) Schematic of electrospinning process. (B) Fluorescence image of tQD-PLLA electrospun fiber. (C) TEM image of tQD-PLLA electrospun fiber cross-section (scale bar 0.5 um). (D) Higher magnification view of tQD-PLLA composite shown in 1C (scale bar 200 nm).

Briefly, tQDs and a solution of poly-l-lactic acid (PLLA) in chloroform were mixed and loaded into a 1-mL syringe with an attached #21 gauge needle. A droplet of the solution was manually ejected from the syringe immediately prior to applying a one kilovolt/centimeter electric field. This caused individual fibers to be formed on the dual rod electrodes[62] (Fig. 2.1). The fibers dried within seconds[71] and were collected for optical and mechanical tests. Fig. 2.1 shows a bright-field fluorescence image of a resulting electrospun fiber, showing red 650 nm fluorescence from the tQDs dispersed throughout the fiber. No diffusion of the fluorescence intensity along the length of the fiber during tests was observed, leading us to conclude that the tQDs are effectively incorporated into the polymer composite structure. The tQDs are not covalently bound to the matrix, nor have they undergone ligand exchange. They are simply incorporated into the polymer via electrospinning with their native hydrophobic ligands. tQDs were incorporated at concentrations of 0, 3.6, 10, 20, and 40% by weight of the PLLA polymer. Fig. 2.1 also shows PLLA-tQD fiber TEM images where the tQDs are forming aggregates in the fiber. tQD aggregates show no preference for the PLLA-solvent interface or interior of the fiber.

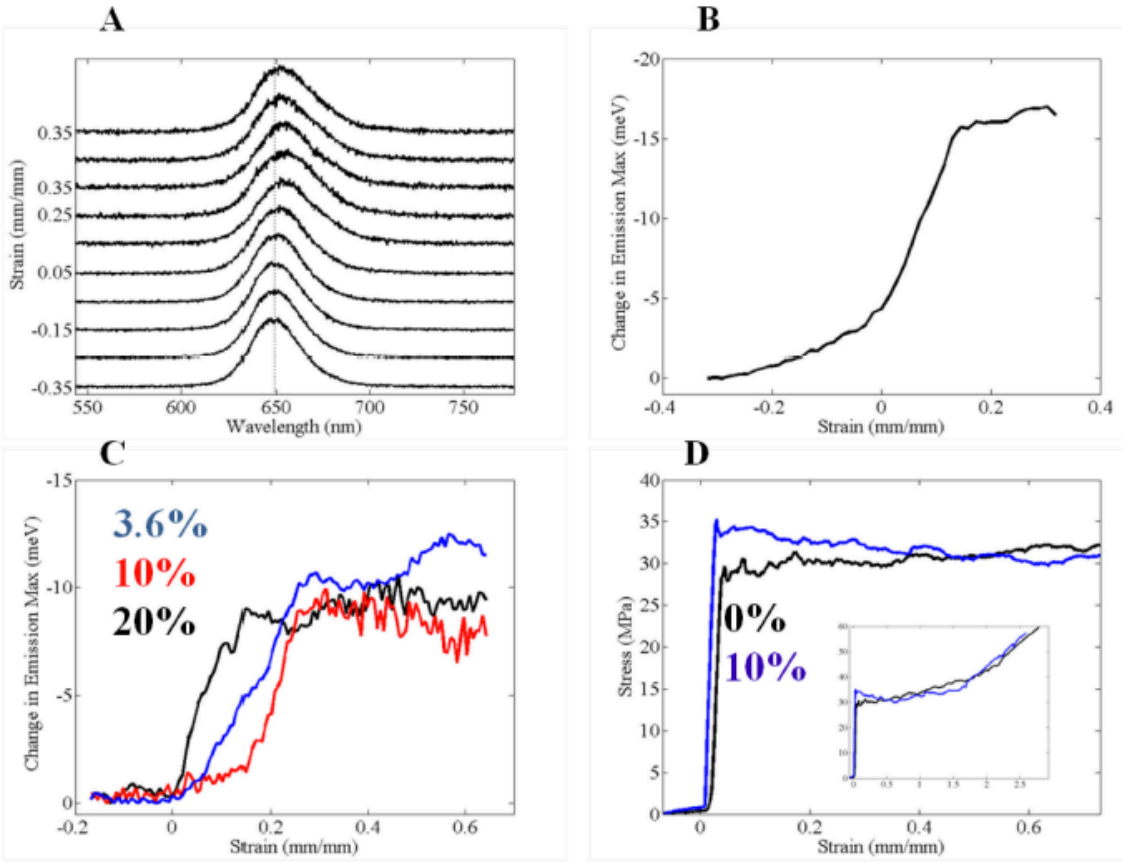

Figure 2.2: Comparison of tQD stress gauge with tensile tester
(A) Selection of raw spectra illustration redshift as a function of strain. (B) Fluorescence tensile curve obtained by fitting and plotting data in A. (C) Illustration of typical fluorescence tensile curves at three tQD loadings. (D) Comparative typical macroscopic uniaxial tensile curve on the same batch of fibers.

2.3: Fluorescence Monitoring of Tensile Deformation

After collection, fibers were mounted onto the piezodrive *in situ* stretcher for fluorescence tests or onto cardboard tabs for mechanical tests. Figure 2.2 shows the raw spectra from a typical fluorescence test, indicating both a redshift as well as an increase in the full-width half maximum (FWHM) of the fluorescence spectrum as a function of stretching. The increase in FWHM (10-20% increase) may be due to a combination of innate spectral line broadening during tetrapod nanocrystal deformation and the natural heterogeneity of strain states within the PLLA polymer fiber. The deformation of the tQD leads to bending of the CdS arms which stretches some bonds more than others; for example, the bonds at the interface between the arm and the CdSe core are more stretched than bonds within the CdSe core. Additionally, the tetrapods at an aggregate edge may be experiencing a different stress than the ones in the middle of a clump or smaller groups of particles in different mechanical contact with the polymer. In the absence of single nanocrystal photoluminescence studies in the fibers, it is not yet known to

what degree deformation of an individual nanocrystal broadens its emission, so the relative contribution of these mechanisms to the FWHM broadening is unclear.

However, the redshift in peak emission clearly tracks fiber deformation. Fig. 2.2 also shows the result of fitting raw spectra to single Gaussians and then plotting these as a function of strain. It indicates an initial slack region followed by a linear elastic region, which then yields and flattens out into a plastic regime. This result matches textbook polymer tensile test graphs[72], as well as our own mechanical tests conducted on the same batch of fibers.

2.4: Concentration Dependence on Sensing Ability

Fig. 2.2 indicates that as the concentration of tQDs in the polymer increases, tQD sensitivity to strain in the fiber increases as evidenced by the average slopes of the linear region. Between concentrations of 3.6 to 20% by weight of the tQDs in the polymer, the average fluorescence slope (ΔmeV/strain) increases 60% from 0.39 to 0.62, though the general shape of the tensile curves is constant. The observed clear distinction between elastic and plastic regimes and consistent curve shape across all particle concentrations in fluorescence tests has not been reported previously[20,29]. Although optical and mechanical tests were conducted on different fibers, all nanocomposite fibers used in comparative tests came from the same batch of electrospun fibers prepared using the same tQDs and polymer precursor solutions.

Fiber-polymer composite studies[73,74] help explain the concentration-dependence illustrated in Fig. 2.2. It is commonly observed in fiber-polymer composites that, provided the fiber/matrix interface is sufficiently strong, the larger the fiber aspect ratio the better the stress transfer and the better the overall composite properties up to a critical length[73,74]. Our observation of a fluorescence slope increase with increased tQD concentration is similar. As the filler concentration increases, the average aggregate size increases and the spacing between aggregates decreases, analogous to a larger aspect ratio in ceramic fiber-polymer composites. This augmented interaction between aggregates leads to a greater stress transfer to the tetrapod phase of the composite. A similar result was recently reported with micron-sized ZnO tetrapods, though in that case a clear distinction between elastic and plastic regimes and good resemblance between tensile and fluorescence curve shapes was only seen at high (50% by weight) ZnO tetrapod concentrations[29]. By contrast, we see clear a distinction between elasticity and plasticity and an optical response approaching that in the mechanical tests at tQD concentrations as low as 3.6% by weight of the polymer. Additionally, in the work with ZnO tetrapods, oscillations were seen in the fluorescence tests at low tetrapod concentrations; this was attributed to non-interlocked tetrapod domains in the polymer matrix[29]. In our case, we find oscillation-free behavior at even the lowest tQD concentrations in the polymer, meaning that interlocking is not necessary to achieve curves with relatively low noise and reasonable accuracy.

A complementary explanation for the particle concentration dependence shown in Fig. 2.2.C is that aggregates near the fiber surface experience increased local strain due to the Poisson effect. PLLA has a Poisson's ratio of ~0.4[75], indicating that it contracts roughly one unit radially for every two units extended axially. Studies indicate that the Poisson's ratio is larger near the surface of a fiber[76]; thus, this contracting force will be greatest at the surface. As the aggregate

concentration increases, the number of aggregates proximal to the outer surface of the fiber does as well. Consequently, more aggregates are present in the region of maximum contracting force near the surface, leading to larger stress transfer and thus better response of the tQD probe. This explanation is consistent with the fact that the average maximum fluorescence peak shift also was seen to increase with concentration from -9.5 meV to -11.3 meV for 3.6% to 20% tQD concentrations by weight in the polymer, respectively, indicating that the sensor becomes more sensitive with increasing concentration.

2.5: Unchanged Mechanical and Structural Properties: A Non-Perturbing Probe

Somewhat surprisingly, the ceramic tQDs do not significantly affect the mechanical properties of the nanocomposite, even at high tQD concentrations. Figure 2.2.C-D shows comparative uniaxial tensile stress-strain curves of electrospun PLLA with and without tQDs and qualitative agreement with optical curves. The inset of Figure 2.2.D shows the full mechanical curves to failure for the same fibers, indicating close agreement between different concentrations, even for 20% by weight tetrapod-fiber nanocomposites. We discuss a possible explanation for the unique non-perturbing behavior of the tQD probe below. The oscillation inherent to the flat region of the polymer curves at high strain is due to plastic deformation; local molecular variations in polymer stress as strands unravel and molecular-scale rearrangements during neck extension. These variations are captured in both the optical and mechanical data.

From the mechanical tests performed on the tensile testing machine on a total of over 70 fibers, there is no significant trend in modulus (measured by taking the slope of the initial linear elastic region of the engineering stress-strain curve), toughness (measured by taking the area under the curve of the entire engineering stress-strain curve), or stress and strain at failure with concentration increased from 0% to 20% by weight of tetrapods in the PLLA polymer. Even at 40%, there is no significant change in elastic modulus although there is a decrease in toughness and other mechanical properties. This is unusual as many composite systems of semiconductor quantum dots[77], micron-scale tetrapods[29], and other polymer-ceramic systems[78] show modulus increases with such weight percent additions, sometimes accompanied by decreases in failure strains and toughness. Although opposite effects have also been observed, it is perhaps surprising that all the tensile mechanical properties remain relatively unchanged with such high concentration of tQDs. However, we believe that this is due to the combination of the weak tQD-polymer interface and PLLA structural variations caused by electrospinning. The poor stress transfer due to the weak interface explains why the measured Young's moduli do not follow a straightforward "rule of mixtures" analysis[79]. Regarding structural variations, PLLA is a semi-crystalline polymer with multiple phases determining its mechanical properties. These phases can clearly be observed as darker and lighter (crystalline and amorphous) regions in our transmission electron microscopy (TEM) images. Small changes in the processing of the electrospinning precursor solutions, such as those introduced by large particle loading, may impact the crystallinity of the resultant fibers. Collection conditions as well as inherent electric field variations across the dual-rod electrodes may also result in structural variations. Accordingly, dynamic scanning calorimetry (DSC) analysis showed significant variation in crystallinity and grain size across samples, but no net effects on the crystallinity and polymer

structural and thermal properties as a function of tQD concentration in the nanocomposite. The result is a material that shows little change in a wide range of mechanical properties even at large particle volume fractions.

2.6: Incomplete Stress Transfer to Nanofiller Sensor

It is apparent from Figs. 2.2.B and 2.2.D that the linear elastic region as measured by the tQD sensor is much broader and covers more strain (6-30% extension) than the linear elastic region as measured by the UTM (which covers between 1-3%). We speculate that this is due to poor stress transfer to the tQD filler. In the case of strong stress transfer, we would expect fluorescence shifts to occur over the same range of strain as seen in the mechanical data as well as significant mechanical property changes in the nanocomposite[80,81]. The poor stress transfer is due to a weak interface between the nanocrystal and the polymer. The PLLA polymer is a hydrophilic aliphatic polyester with hydrogen bonding between the chains. The tQDs, with their native hydrophobic ligands, cannot participate in the hydrogen bonding. This unfavorable ligand-polymer interaction leads to the observed tQD clusters in the polymer matrix. Prior demonstrations of the tQD support the idea of partial stress transfer to the particle. Previously, tQDs were added to hydrophilic polymers, such as Nomex, through diffusion after application of a droplet of particle solution[20]. Diffusion likely creates a weaker particle-polymer interface than electrospinning and explains why a smaller maximum particle shift was seen in previous work[20]. This suggests the tQD could also be used to optically probe the particle-polymer interface strength in composite materials.

Despite the incomplete stress transfer to the particle phase, the tetrapod fluorescence still clearly responds to fiber deformation. This demonstrates the tQD's usefulness in reporting phase-specific mechanical information in composite materials. The UTM load cell senses the macroscopic strain, while the tQD is only sensitive to nanoscale deformations that introduce a strain in the CdSe/CdS nanocrystal lattice. These latter deformations may arise from nanoscale particle-particle interactions (inter- and intra-aggregate interactions) or direct nanoscale particle-polymer interaction, but not from purely polymer molecular modes of deformation such as amorphous twist-tie chain unraveling, backbone covalent bond stretching, and others[72]. The phase-specific probing behavior of the tQD helps explain the differences between optical and mechanical testing.

2.7: Stress Relaxation and Cyclic Deformation

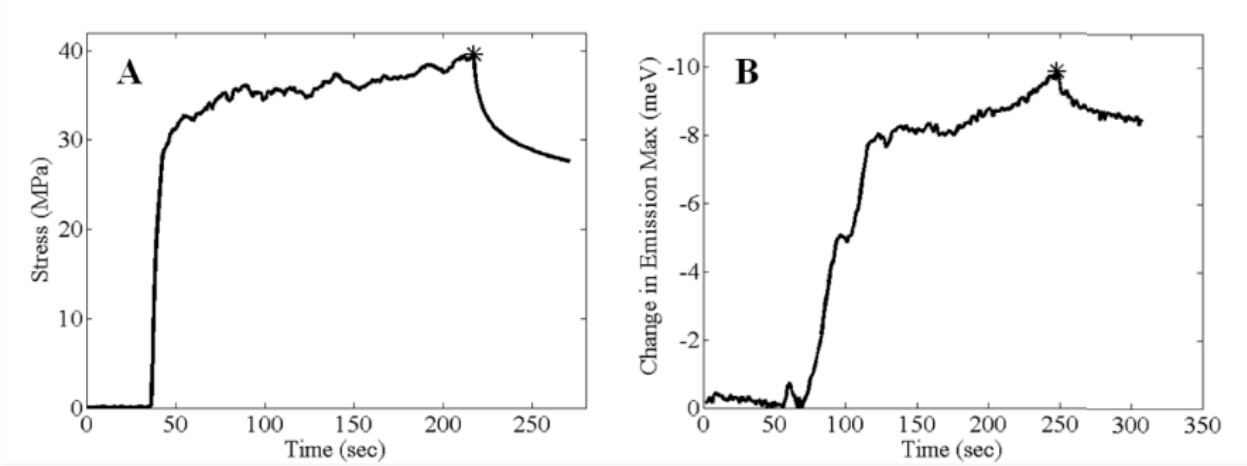

Figure 2.3: Measuring stress relaxation using tQDs
*(A) Macroscopic uniaxial tensile mechanical test illustrating stress relaxation. (B) Fluorescence test data obtained under same mechanical test conditions. * indicates where strain was held at 77%.*

In service, parts often undergo more complex stress-states than pure tensile elongation, such as stress relaxation and hysteresis. These more complex behaviors are of key importance to understanding polymer dynamics. Therefore, with an eye towards applications and advanced fundamental studies, we also examined stress relaxation and hysteresis in the nanocomposite, both optically as well as mechanically. To the best of our knowledge, this has never been mapped using self-sensing nanoscale sensors embedded into a material. Fig. 2.3.A depicts the results of a mechanical tensile test in which a fiber containing 10% tetrapods by weight was stretched to 77% strain and held there for approximately 53 seconds. Stress is plotted as a function of time and shows an exponential fall-off associated with stress relaxation in the polymer[82]. Figure 2.3.B illustrates a fluorescence test performed under identical strain rate and holding conditions as the mechanical test. The same distinct exponential fall-off in stress relaxation is seen. The stress relaxation tests in the UTM were performed on 5 fibers of each tQD concentration (15 fibers total) and no difference in load relaxation properties was observed as a function of concentration. The mechanical stress relaxation behavior showed a 28.8±0.8% 30.2±0.7%, and 29.9±1.38% relaxation for fibers containing 3.6%, 10%, and 20% tetrapods by weight, respectively. The average over all 15 samples was 29.6±1.13% relaxation. By contrast, the average over 45 fiber samples of stress relaxation measured optically was 20.9±6.24% relaxation. Given that the mechanical test measures macroscale stress relaxation while the tetrapod sensing of stress relaxation originates from local nanoscale polymer deformations, the degree of agreement between the two measurements is striking and demonstrates that the tetrapod can be an effective nanoscale sensor for stress relaxation, in addition to tensile properties. This may be useful for a variety of applications as it demonstrates an optical means of determining stress relaxation prior to failure in structural materials. We observed a faster mechanical stress relaxation rate, consistent with the incomplete stress transfer to the tetrapod filler phase. In the case of the tQD-PLLA polymer nanocomposite, the load sensor is the filler

phase and therefore only measures a fraction of the load felt by the polymer matrix. The smaller exponential stress falloff measured optically is thus in accord with the broadness of the linear response of the tQD as compared to that measured by the tensile testing machine, and further supports our proposed stress transfer explanation of differences between the two tests.

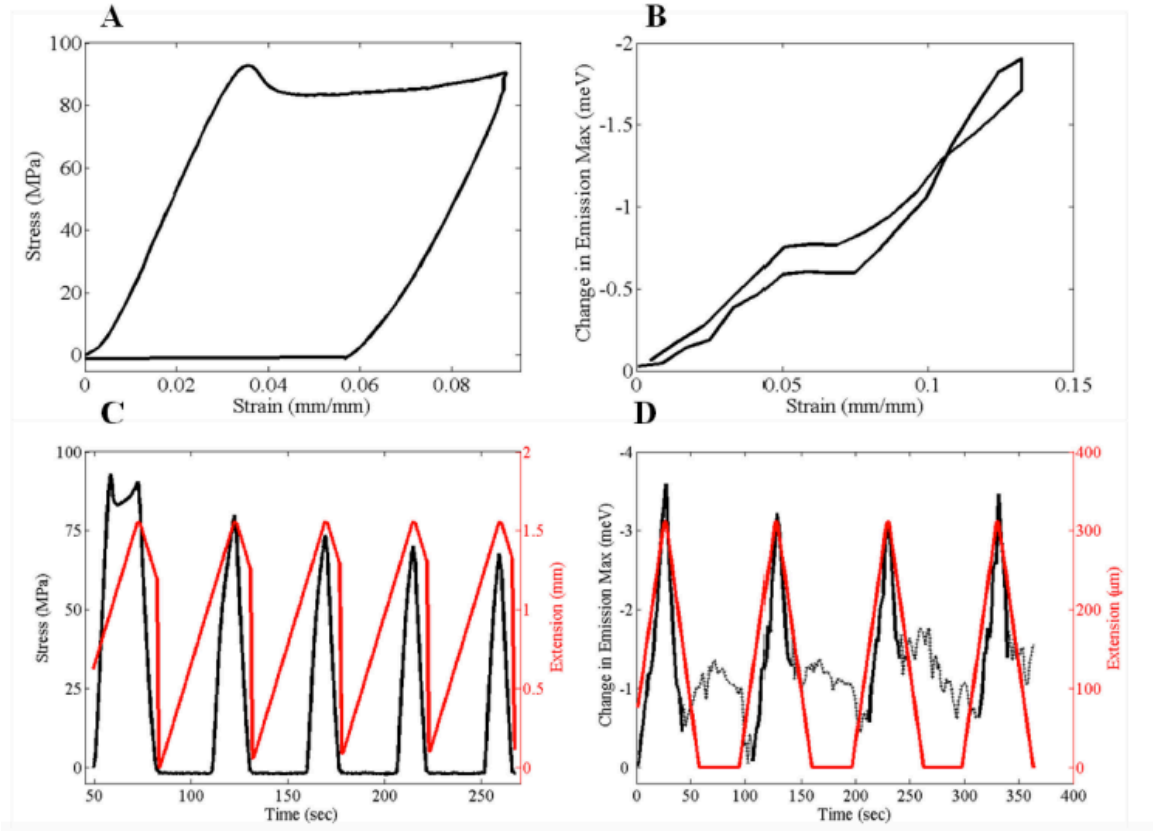

Figure 2.4: Measuring cyclic deformation using tQDs
(A) Mechanical hysteresis loop illustrating plastic deformation and accompanying energy loss. (B) Fluorescence 'hysteresis' curve obtained under the same mechanical testing conditions. (C) Hysteresis loops from trials shown in part A plotted versus time. (D) Fluorescence 'hysteresis' loops of data from trials in plot B plotted versus time. Dashed regions indicate periods where fiber was not in focus due to slack from plastic deformation.

We also used the tQD as a probe for sensing the response of the single PLLA fibers to cyclic loading, again as compared to mechanical tests, and found telling differences between the hysteresis curves obtained via the two methods. Fig. 2.4.A shows a hysteresis loop done on a 10%-tetrapod-PLLA composite fiber measured mechanically. The fiber was stretched to approximately 10% strain and returned to zero strain at the same strain rate; as before the same strain rates and test conditions were used with both sets of tests. The fiber shows clear hysteresis in the first cycle of the mechanical test (Fig. 2.4.A), but does not show hysteresis in the first optical test cycle (Fig. 2.4.B). If taken as a sensor of the polymer matrix, the tetrapod is reporting that some of the polymer plastic deformation is elastic. We believe that this again indicates that the tQD sensor is, in the PLLA nanocomposite system, reporting the stress that is transferred to

the particle phase rather than the stress felt by the matrix. Furthermore, the fluorescence shift is based on an elastic deformation of the tQD crystal lattice[52,83] and is not expected to show hysteresis[54].The complete recovery of the initial width and position of the fluorescence signal also indicates the lack of residual stress in the tetrapod. Possibly, the poor particle-polymer interface, and the accompanying aggregation, may limit stress transfer to the tetrapods and prevent permanent deformation of the tetrapod probe.

Figures 2.4.C and 2.4.D represent the trials shown in Figures 2.4.A and 2.4.B respectively, only now as a function of time. In these plots, the clear resemblance between the latter cycles is shown, whereas the first cycle again displays plastic deformation. Figure 2.4.D also illustrates a level of baseline optical noise present in between optical test cycles. The noise is due to the fiber coming out of focus between cycles. Upon plastic deformation, the fiber length increases, and so upon returning to zero strain between cycles, it goes out of focus.

As the cyclic deformation has nearly no hysteresis in the tetrapod fluorescence shift, no energy is dissipated in the tetrapods even when a great deal is lost in the polymer; this is evident through the degree of plastic deformation present in the mechanical hysteresis curves. These observations of hysteresis imply that in composites characterized by weak nanofiller-polymer interfaces, such as the nanocomposite material presented here, failure occurs due to cracking in the polymer matrix or particle-polymer interface rather than within the tetrapod nanoparticle phase. Through hysteresis data, the tQD therefore provides a simple imaging technique for determining the source of failure in a nanocomposite.

2.8: Conclusion

In summary, we have demonstrated that electrospun tQD-polymer composites provide a fluorescence-based measurement of tensile stress or strain in good agreement with results from traditional uniaxial tensile testing. We have shown that tQds are capable of fluorescently reporting the stress on a nanoscale volume element of a nanocomposite material. Based on this work, several key conclusions can be made. The elastic and plastic regions of deformation during extension are easily observed as a shift in the fluorescence of the tQD even at low particle concentrations, although a greater fluorescence shift per unit strain is observed with increasing concentration. Despite aggregation and poor stress transfer, the tQD shows close agreement with traditional tensile measurements. Far from problematic, this aggregation and accompanying weak interface may present an advantage; by limiting stress transfer to the tQD, it ensures accuracy and elasticity (recoverability and recyclability) by preventing plastic deformation of the tetrapod sensor. The tQD acts as a non-perturbing probe since electrospinning provides a straightforward means to form polymer-nanocrystal nanocomposites across a wide range of particle concentrations without adversely affecting the mechanical properties of the PLLA matrix used in this study. We further show the capability of the tQD to monitor not only simple uniaxial stress, but stress relaxation and behavior under cyclic varying loads.

2.9: Materials and Methods

Synthesis of CdSe-CdS tQDs: CdSe-CdS core/shell tQDs were prepared in-house via established methods[49]. The tQDs had average arm length 22 ± 4.5 nm and average diameter 4.0 ± 0.75 nm.

Preparation of tQD-PLLA Polymer Solutions for Electrospinning: PLLA (100,000 g/mol molecular weight) was purchased from ShenZhen ESUN Industrial Co. Ltd., and dissolved in chloroform (Sigma Aldrich) to create solutions of 20% PLLA by weight in chloroform. tQDs coated with native hydrophobic ligands (no post-synthetic modification) were dissolved in chloroform and added to the 20% PLLA solution to create solutions of 12% PLLA by weight in chloroform with 3.6%, 10%, 20%, and 40% tQDs by weight of PLLA.

Electrospinning of tQD-PLLA Composite Fibers*:* Electrospinning was performed using a bias of 15 kV between the collector and syringe needle and collector-syringe needle distance of 15 cm. Needles purchased from Nordson corporation (part number 7018225, 38.1 mm gauge length) were used. 0.1-0.2 mL of solution was loaded into the syringe, and a large droplet of solution was manually ejected immediately prior to turning on the power supplies. Single fibers of diameter 2.5-10 microns were fabricated using the collector design of Li et al[62] while dynamic scanning calorimetry samples were fabricated using a random fiber network deposited onto a single metal rod under the same electric field conditions. For transmission electron microscopy (TEM) studies, single aligned fiber arrays were wound around a microtomable epoxy substrate and supper-coated with 15 nm of gold[84,85]. Single fibers were removed from the double-rod collector using twisted pipe cleaners coated with double-sided tape, and subsequently taped and glued directly onto the Piezodrive stretcher for fluorescence monitoring or onto small cardboard tabs (10 mm x 5 mm) for mechanical tests.

Tensile Testing and Optical Diameter Measurements*:* Single fibers were removed from the double-rod collector using twisted pipe cleaners coated with double-sided tape, and subsequently taped and glued with epoxy directly onto small cardboard tabs (10mm x 5mm) for mechanical tests. The diameters of the fibers were imaged and photographed using a 63x objective lens on a standard optical microscope (QCapture camera and QImaging software) which was calibrated using a TEM grid (11.85 pixels/micron). The fiber diameters were analyzed using ImageJ. Tensile testing was performed using an Agilent T150 nanomechanical tensile tester. The strain rate was set to 4e-3 for all runs, and mounted in the tensile tester using standard pivot grips. The average fiber diameter measured over 20-25 samples was 6.6 ± 2.2, 5.1 ± 0.7, 4.7 ± 2.2 um, and 4.7 ± 1.6 um for 0, 3.6, 10, and 20% tQDs respectively and the gauge lengths, measured with digital calipers, fell between 6-10 mm. For standard tensile mechanical tests, we conducted a total of 20-25 tests per sample of 0%, 3.6%, 10%, and 20% loading by weight of tetrapods, rods, or dots in the PLLA polymer. For load relaxation tests, performed on five samples for each concentration, the sample was held at a maximum strain of 77% for 53.25 seconds. For hysteresis, performed on five 10% tQD-PLLA samples, 5 cycles to a maximum strain of 13% were run continuously and the samples had an average diameter of 3.9 um. For modulus calibration, a total of 22 fibers for the 3.6%, 25 samples for the 10%, and 20 samples for the 20% fibers were used.

Piezodrive in Situ Fiber Stretcher: In order to monitor the fluorescence while stretching the single fibers continuously, a piezo-stretcher mounted via screws on a metal platform was used;

the platform had a hole to allow the laser to reach the sample. A piezodrive (part number O-103-01) and D-drive controller were purchased from Piezosystems Jena. The piezodrive was controlled using a function generator (Agilent/HP 3314A, 0.001 – 20 MHz) and the triangle wave signal was monitored using a 500 MHz oscilloscope. The gauge length for all optical tests was 1.8 mm. The piezodrive was calibrated to move at a strain rate of approximately 4e-3 for all tests. Strain was calculated by dividing the total range of motion of the drive by the fiber gauge length. The piezodrive was screw-mounted on a 0.5" steel platform (6x8") with a hole for laser passage for stability during stretching. For hysteresis, a maximum strain of 13% was used, and a total of four cycles were run per sample, while for load relaxation, a maximum strain of 77% was used and one cycle was run per sample, and the sample was held at the maximum strain for 53.25 seconds. The nanocrystal fluorescence was excited with a 488-nm Ar^+ laser (Lexel Laser, Inc., 95) with 1-W power and 250-μm spot size at the sample. Brightfield and fluorescence images were taken with a digital microscope camera (Paxcam 2+). The fluorescence spectra were monitored using a home-built inverted fluorescence microscope with a spectrometer (Acton Research Corporation, SpectraPro-3001) and CCD detector (Princeton Instruments, Model 7509-0001). Exposure times of 1 s were used to collect spectra with a 0.6 s lag time between frames. Approximately 190 spectra were collected for each load relaxation curve and 220 for each series of 4 loading cycles. Fluorescence spectra were collected over the area of the laser spot and fit to single Gaussians. Change in emission was defined as the difference between the peak position at time t and the peak position at zero strain. Stress relaxation rates were determined by fitting the emission shift versus time to a single exponential decay: $\Delta\text{Emission}(t) = Ae^{-\lambda t}$. For mechanical tests, stress was substituted for emission shift. Optical decays were fit to a series of 35 spectra over 53 sec. Mechanical decays were fit to approximately 530 load measurements over 53 sec. Optical stress relaxation data was collected on 13, 14 and 12 fibers of 3.6%, 10%, and 20% tetrapod load by weight, respectively.

Transmission Electron Microscopy Imaging and Sample Preparation: Epoxy (Araldite 502, Electron Microscopy Sciences) was formed into a thin plate by curing overnight at 60C in a shallow dish. The electrospun fibers sample were then wrapped around these substrates and sputter -coated with around 15-20 nm of gold using a Desktop II Denton sputter coater. They were then embedded in more epoxy stained with rhodamine 6G (Sigma Aldrich) and cured overnight at 60C. Thin sections approximately 60 nm in thickness were cut using an RMC MT-X Ultramicrotome (Boeckler Instruments) and picked up from water onto copper TEM grids. The thin sections were imaged using an FEI Tecnai 12 at an accelerating voltage of 120keV or an FEI Tecnai G2 at an accelerating voltage of 200 keV.

Dynamic Scanning Calorimetry Experimental Parameters and Data Analysis: Samples were heated to 200C at a rate of 20C/min on a TA Q200 DSC with an RCS 40 Refrigeration unit. Analysis was subsequently carried out using the TA Universal Analysis software package.

Chapter 3 : Mechanisms of Local Stress Sensing in Polymer Films Using tQDs

3.1: Introduction

Prior studies on the tQD as a polymer stress sensor, including those in the previous chapter, have been limited by low sensitivity and the detection of only tensile stresses, and no self-reporting of local composite morphology.[18,20] Furthermore, sensing was also only demonstrated in polymer fibers, rather than films,[18,20] and was restricted by an inability to correlate optical and mechanical data as these measurements could not be performed simultaneously[18].

Here, we present the tQD as a detector of nanoscale compressive and tensile stress when embedded into widely-used, low-cost smart structural block copolymer films. We perform optical sensing during mechanical testing in real time and show quantitatively the reasonable degree of matching between optical and mechanical curves. For the first time, we illustrate sensing in terms of both photoluminescence emission-maximum and full-width half maximum (FWHM). The tQD responds to stress via changes of its energy band gap[54], with the response coming mostly from its CdSe core due to type I band alignment between the core and the CdS arms.[86] Tensile stress decreases the band gap by pulling apart the bonds in the tQD core, while uniform compression increases the band gap by moving the ions in the CdSe core closer together[54]. The photoluminescence emission spectra measured from tQDs embedded in the polymer matrix is then shifted to higher or lower frequency (blue- or red-shift respectively) allowing for a direct measure of local stress. We show that tensile stress applied to densely-packed tQDs in polymers results in a blue-shift of the tQD photoluminescence emission maximum due to uniform compression of tQD cores, while tensile stress applied to loosely-packed tQDs in polymers results in a red-shift of the tQD photoluminescence emission maximum due to a net core tension. This phenomenon arises from the unique ability of tQDs to self-report subtle changes in nanoscale dispersion and related changes in macroscopic composite mechanical properties, with a switch in optomechanical response from red-shifting to blue-shifting when tQDs are in direct contact. A polymer-embedded sensor that can self-report its own dispersion would be of broad utility for nanocomposite design, and to the best of our knowledge, has never been reported.[57,87]. Due to the unique stress amplification effects of the tQD, the film sensors have two orders of magnitude higher stress response than bulk CdSe[29,32,34,88,89]. Using density functional theory, finite-element modeling, and experimental techniques such as transmission electron microscopy (TEM), electron tomography, characterization of fluorescence as a function of tensile stress, time-resolved photoluminescence spectroscopy, atomic force microscopy (AFM), and soft-x-ray scattering, we reveal the nanoscopic origins of the tQD photoluminescence shifts. Furthermore, we show that tQDs do not degrade the mechanical properties of the polymer films and have unchanged photoluminescence properties even after a year of storage in air; moreover, the film preparation method is scalable to industrial processing. The tQD sensor can be customized to sensing local tension or compression by changes in room-temperature processing. tQDs provide a highly sensitive material to potentially monitor stress distributions around cracks in structural nanocomposites for in service

applications, and can potentially be implemented *in the field* using low-cost, portable equipment. As previous work has shown the ability of spherical nanoparticles to diffuse to growing cracks in materials and diminish their ability to propagate[17], the findings of this work could possibly allow for diverse 'smart', dispersion-reporting, self-healing structural tQD-spherical nanoparticle-polymer nanocomposites that can sense local and overall composite mechanics as well as potentially detecting and preventing their own fracture[20,45,57].

3.2: Mechano-Optical Sensing Behavior of tQD Nanocomposite Films

The fluorescence properties of both films were studied under tensile deformation using an inverted fluorescence microscope (Fig. 3.1). Understanding of the tQD stress response requires knowledge of agreement between optical and mechanical tests. Here we examine the concept of tQD mechano-optical sensing by coordinating mechanical and optical data acquired simultaneously. Our composites were deformed uniaxially to a maximum strain of 60% and held to evaluate stress-relaxation behavior.

The mechano-optical sensing behavior, depicted in Fig. 3.1, shows a fluorescence shift of the tQD-SEBS composites in the compression-sensing and tension-sensing films as a function of applied strain, along with the corresponding mechanical loading curves (black lines). The results of peak position and FWHM for compression-sensing nanocomposites (Fig 3.1.C-D) indicate excellent agreement between the mechanical loading curve and the optical sensing curve. Most of the emission maximum shift occurs in the elastic region, in which a slope of 8.6 ± 0.9 meV/MPa is measured as well as a maximum optical shift of 4.5 ± 0.4 meV. The fluorescence curve additionally shows variation in the nonlinear region, and matches the exponential behavior of the mechanical stress relaxation well.

We also see fairly good opto-mechanical agreement in the tension-sensing composites (Fig. 3.1.G), although not as good as in the compression-sensing composites (Fig. 3.1.C). The maximum fluorescence red-shift occurred mainly in the elastic region, which had a slope of -2.4 ± 0.3 meV/mPa and a maximum optical shift of 1.3 ± 0.14 meV.

We find that for compression-sensing films, the FWHM of the spectra follows the stress-strain curve of the composite (Fig. 3.1.D). Additionally, the FWHM sensitivity in stress and strain, -39 ± 5 meV/MPa and -300 ± 30 meV/strain, respectively, is significantly higher than previously reported tQD emission maximum response sensitivity[20,44]. This additional sensing mode is not observed in any of the tension-sensing films (Fig. 3.1.H) or in any previous studies in tQD fiber composites[20,44]. Unlike in the compression-sensing films, and as in previous work, the photoluminescence FWHMs in tension-sensing films exhibit a slight increase (Fig. 3.1.H) but do not track the stress-strain curve[20,44].

All sensitivities, or pressure coefficients, reported in units of shift/stress (meV/MPa) show significant improvements over the values reported for bulk CdSe[88,89]. This is perhaps due to the unique geometry of the tQDs, in which the CdS arms act as antennas that amplify and transfer stress from the environment to the CdSe core. Indeed, this was also seen in our finite-element simulations, as discussed below**.** Our tQD films sense stress with an optical deformation

response three orders of magnitude more sensitive than previous tQD sensors[18], making them equal or better in sensitivity than several other key local stress-sensing technologies.

The *sensitivity* of a probe can be defined by $S = (R/R_o)P$, a common index of quantification for most sensing technologies, where R is the change in sensor response, R_o is the baseline response, and P is the phenomenon under study, in this case, stress. In this work, we now see much improved sensitivity, making the tQD comparable or superior in sensitivity to other key local stress-sensing technologies reported to date. The compression-sensing tQD-film nanocomposites have a stress sensitivity of 4.5e-6 kPa^{-1}, which is three orders of magnitude higher than previous tQD sensors[18,20] and similar to or higher than common mechanochromic dyes[90,91], gold nanoparticle chain plasmonic sensors[34], and stress-sensitive metal nanoparticles[30], which have sensitivities of 1.9e-5, 4.1e-10, and 2.2e-6 kPa^{-1}, respectively. The tQD is thus a complementary method to these existing techniques, with the added advantage of full cyclability, adaptability to almost any polymeric matrix because of its colloidally stable, readily tunable ligand coating, and lack of degradation to the mechanical properties of the host material.

The films exhibited nearly identical optical and mechanical properties even after a year of storage in air. The sensing is very repeatable; 20+ cycles of stretching to ~60% strain performed on the same sample led to nearly identical sensor responses with a return to the same baseline fluorescence FWHM and emission maximum in-between tests. This likely indicates that the tQDs are experiencing fully elastic deformation during the stress-sensing in the polymer[52]. Compared to control samples, the ductility and toughness of the compression-sensing and tension-sensing films were unchanged.

We investigated the possibility that the blue-shift under tension could be due to better Forster resonance energy transfer (FRET) efficiencies in close-packed aggregates. However, this is unlikely as we found no difference in photoluminescence rise time or initial lifetime decays[92,93] between compression- and tension-sensing films.

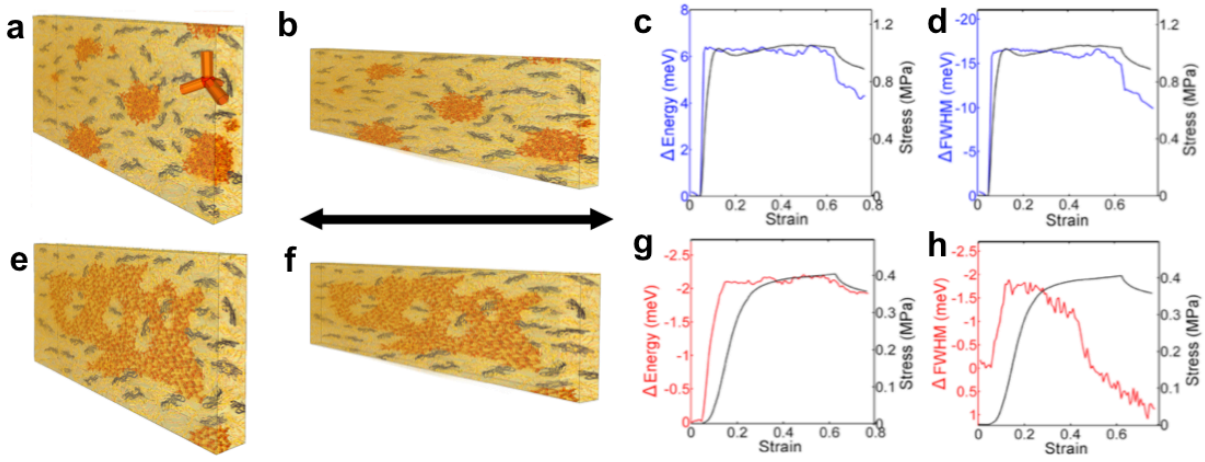

Figure 3.1: Schematic microstructures and mechano-optical stress-strain curves of tQD-nanocomposite films

a,b. Schematics of the microstructures of compression-sensing film (a) before and (b) after application of stress. Yellow regions represent PE-B, black regions represent PS, and orange regions represent tQDs. c,d. Result of simultaneous fluorescence (blue line) and mechanical test (black line) for c. emission maximum and d. FWHM. e,f. Schematics of tQD-SEBS tension-sensing film (a) before and (b) after application of tensile stress. g,h. Result of simultaneous fluorescence (red line) and mechanical test (black line) for g. emission maximum shift and h. FWHM shift for tension-sensing film. Black double arrow indicates direction of applied tensile stress.

3.3: Structural Characterization of tQD Nanocomposite Films

The different, opposite, photoluminescence shifts in tension-sensing and compression-sensing composites are rather striking since the films only differ in their drying time. To investigate whether the microscopic structural differences between these two films were responsible for their disparate sensing behavior, transmission electron microscopy was used to determine their microstructures. The images shown in Fig. 3.2 show that the two films exhibit very different morphologies. Qualitatively, the compression-sensing tQD contains densely-packed aggregates which appear darker than the tension-sensing aggregates in the TEM images. The tension-sensing aggregates are less dense and have a large number of 10 - 500 nm diameter inter-tQD regions, as seen in Figs. 3.2.B and 3.2.D. Due to the fast diffusion constant of the polymer chains in solution during drying ($>10^{17}$ cm^2/sec[94]) and the rate of the drying processes employed, these regions are likely filled with polymer. This was confirmed by electron tomography (Fig. 3.3) which shows that the inter-tQD regions are filled with matter consistent in contrast with the polymer material outside the aggregates. Figure 3.2.G shows histograms of aggregate diameters for compression-sensing and tension-sensing aggregates, respectively, from several TEM images. In general, tension-sensing aggregates have a diameter some two times greater than compression-sensing aggregates. Figure 3.2.G also shows that the quickly-dried tension-sensing material contains some large aggregates as indicated by the asymmetric histogram with a large tail, while the slowly-dried compression-sensing aggregates have a more symmetric size distribution. The change in packing density that results in a switch from red- to blue-shifting, or tension- to compression-sensing, is accompanied by a Young's modulus increase of a factor of two. Thus, tQDs do not only report subtle changes in the nanoscale dispersion of the composite filler phase, but also can serve as a visible-light indicator of associated changes in mechanical properties.

Small angle x-ray scattering (SAXS) experiments were carried out to provide statistical information as support to TEM and AFM results. Conventional SAXS relies on the electron density contrast between materials. Since the tQD has much higher electron density compared to the polymers, the SAXS signal was dominated by the tQD aggregates and it was not possible to observe the polymer phase separation. Therefore, resonant soft x-ray scattering (RSoXS) was used to characterize block copolymer morphology in compression-sensing and tension-sensing films. The RSoXS experiment was carried out at BL11.0.1.2 at the Advanced Light Source,

Lawrence Berkeley National Lab. Using x-rays with photon energies close to the absorption edges of the constituent atoms in the material, RSoXS combines conventional x-ray scattering with the chemical sensitivity provided by soft x-ray spectroscopy. By turning the x-ray energy, the contrast between materials as well as sensitivity to a specific phase in the complex system can be adjusted. Thin film samples were obtained by cryo-microtomy, and cryo-microtomed films were supported by silicon nitride membranes (Norcada). The sizes of the samples were ~ 100 μm by 300 μm with thickness ~70-90 nm. RSoXS was measured in transmission geometry and the data was collected with an *in vacuo* CCD camera (Princeton Instruments) at a series of photon energies near the carbon edge. Strong scattering peaks was observed at ~ 285 eV, which is the resonant energy for the polymers where the contrast between two polymer blocks was enhanced. For the control samples (polymers dried at the two drying speeds described in the main text without tQDs), the scattering features corresponding to the block copolymer phase separation were observed at all energies. However, for the samples containing tQDs, the block copolymer peaks were only observed at the resonant energies.

For the tension-sensing sample, the primary scattering peak is observed at 0.023 $Å^{-1}$, which corresponds to a real space size of ~ 27 nm. This size is corresponding to the block copolymer phase separation. For the tension-sensing sample, the primary peak is observed at ~ 0.025 $Å^{-1}$, which corresponding to a 25 nm spacing. For the control samples with both fast- and slow-drying condition, the primary scattering peaks were at ~0.027 $Å^{-1}$, corresponding to a 23 nm spacing, which agrees well with SAXS and TEM results. The peak positions were determined by fitting the primary peaks with a Gaussian profile. The full-width half maximum (FWHM) for the tension-sensing, compression-sensing, and control films were 0.0071483, 0.006766, 0.011644, 0.0082148, respectively. The FWHM of the primary scattering peak in the scattering profile is a good indication of the ordering of the block copolymer. A smaller full-width half maximum is indicative of better ordering. A slower drying condition results in slightly better ordering for both the tQD sample and the control samples. While these differences are apparent, it is not clear how they could be responsible for the disparity in sensing behavior (i.e., compression-sensing or tension-sensing) observed in the two films.

Traditional TEM projection images are sufficient to determine the large-scale (>100 nm) porosity inside the aggregates, but the overlap of many tQDs in projection obscures their 3D distribution and the small-scale (<10 nm) inter-tQD regions. We utilized STEM electron tomography to determine the internal distribution of the tQDs and polymer inside of the aggregates. Fig. 3.3 shows images of isosurface renderings of 3D electron tomography reconstructions for both the compression-sensing and tension-sensing composites. The tomography was performed using cryo-microtomed cross-sections with a thickness (~70-90 nm) smaller than the diameter of the aggregates (~150 nm). The tomographic images revealed small regions of polymer ~10 nm in diameter which were inside the aggregates and not visible in the TEM projection images (Fig. 3.2). The analysis of small-scale porosity from each individual slice of the tomography reconstructions showed that the volume ratios of tQD/polymer (which we term tQD aggregate fill fraction, or packing density) in the aggregates were 50% ± 5% and 25% ± 2% for compression-sensing and tension-sensing aggregates, respectively. This small-scale porosity can be viewed as an approximation of the distance between adjacent tQDs, as

tQDs have arm lengths of 26 ± 3 nm. These results illustrate that individual tQDs are about a factor of two farther apart in the tension-sensing aggregates than in compression-sensing aggregates, and that the tension-sensing aggregates have a factor of two times more polymer inside of them in terms of small-scale inter-tQD regions. They also indicate that, in the aggregates, the tQDs are in direct contact, separated only by their thin outer ligand coating[95-97]. Only red-shifts were seen at a variety of tQD packing densities below 50%, including homopolymers and cases in which tQDs are singly dispersed. Due to the colloidal nature of tQDs, and their smart ability to self-report whether they are in direct contact, they potentially could enable auto-responsive, multifunctional structural nanocomposites that would self-predict local and bulk mechanical properties as well as impending fracture.

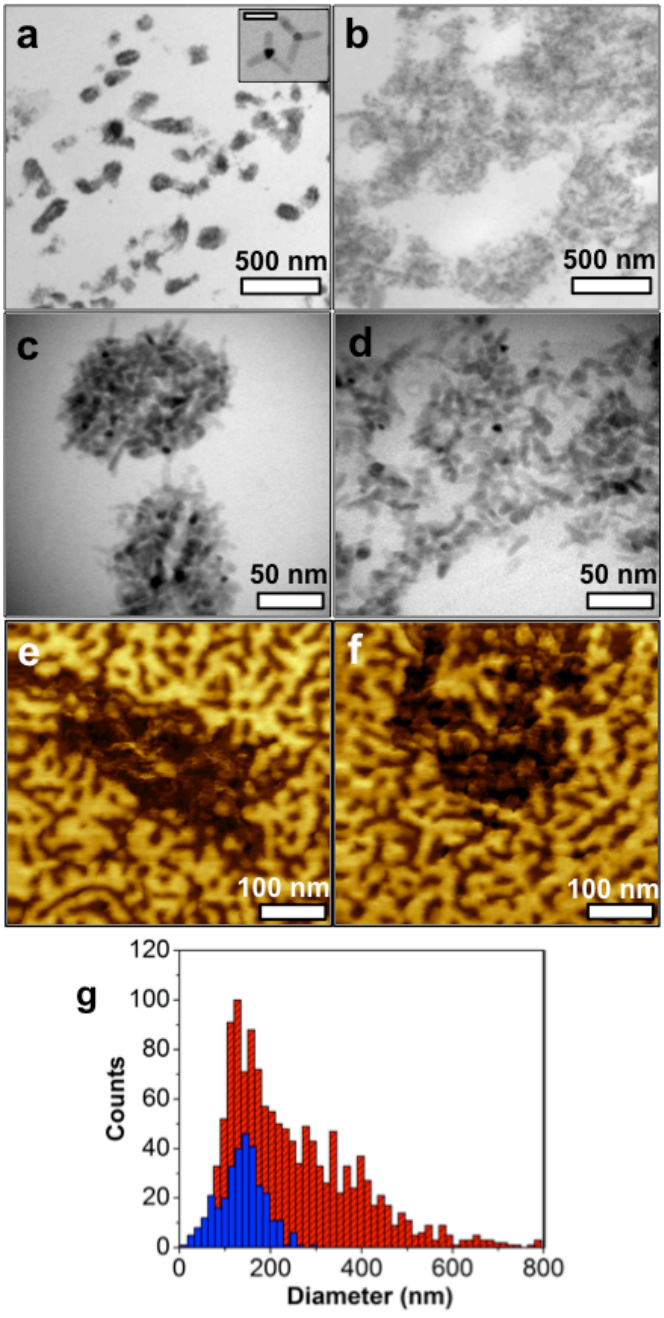

Figure 3.2: TEM and AFM of tQD-nanocomposite films
a-b. *Low magnification TEM micrographs of* ***a.*** *compression-sensing and* ***b.*** *tension-sensing films. Inset to (a) indicates tQDs before polymer encapsulation. Inset scale bar is 40 nm.* ***c.*** *Higher resolution TEM images of compression-sensing and* ***d.*** *tension-sensing films showing that they are composed of tQDs.* ***e-f.*** *AFM micrographs of* ***e.*** *compression-sensing and* ***f.*** *tension-sensing films.* ***g.*** *Size distributions of diameters of tQD aggregates in compression-sensing and tension-sensing films. Blue and red histograms represent size distributions for compression-sensing and tension-sensing films respectively.*

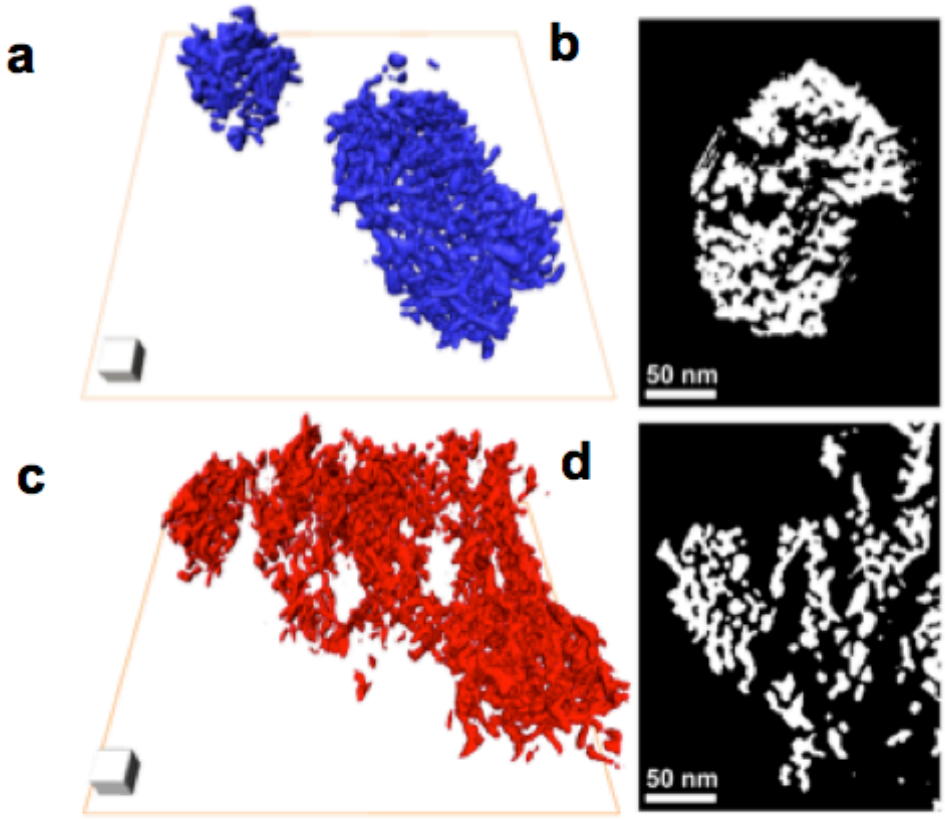

Figure 3.3: Electron tomography of tQD-nanocomposite films
a, b. *Perspective image of isosurface reconstruction of tension-sensing and compression-sensing aggregates produced by electron tomography. White scale cube has 25 nm sides.* ***c, d****. Thresholded 1.13-nm slices of the tomogram representative of the internal structure of the compression-sensing and tension-sensing aggregates, respectively.*

3.4: Simulations of tQD Stress Response

Simulations done over multiple length scales (atomistic density functional theory and micromechanical finite element simulations) are explored to divulge the mechanistic origins of the tQD stress response.

3.4.1: Atomistic Electronic Structure Calculations

Having shown how the aggregates differ structurally, we now use electronic structure calculations to illustrate the underlying mechanism of photoluminescence shifts due to an applied mechanical stress. We performed atomistic density functional theory simulations on tQDs with zinc-blende CdSe cores of 2.8 nm, wurtzite CdS arms of 4.2 nm in length and 1.9 nm in diameter; containing 4245 atoms with chemical formula $Cd_{272}Se_{297}/Cd_{1132}S_{1116}$, with pseudo-hydrogen passivation. We found that both the conduction band minimum state and valence band maximum state are located in the CdSe core, in agreement with experiments[86]. To simulate stressed tQDs, an atomistic valence force field model[98] was used to calculate the atomic positions under different stresses. The different stress states include uniform bond distance scaling (isotropic compression and tension) and uniaxial pushing or pulling at the tips of the four arms (uniaxial compression and tension) (Fig. 3.4).

Only the uniform, volumetric compression case results in a blue-shift. Among the red-shift cases, the situation most relevant to the experiment is uniaxial tension. The local strain of the tQD under uniaxial tension is shown in Fig. 3.4.D. Near the CdSe core, there are both positively and negatively dilated regions. This makes the red-shift relatively small. Considering that 2.5% strain was applied, which is likely much higher than the experimental tQD strains due to imperfect stress transfer to the tQD[57], the theoretically obtained band gap changes were much higher than the experimentally observed shifts. In summary, the theoretical results revealed that only deformations that caused a net decrease in volume of the CdSe core produced a blue-shift of the energy levels.

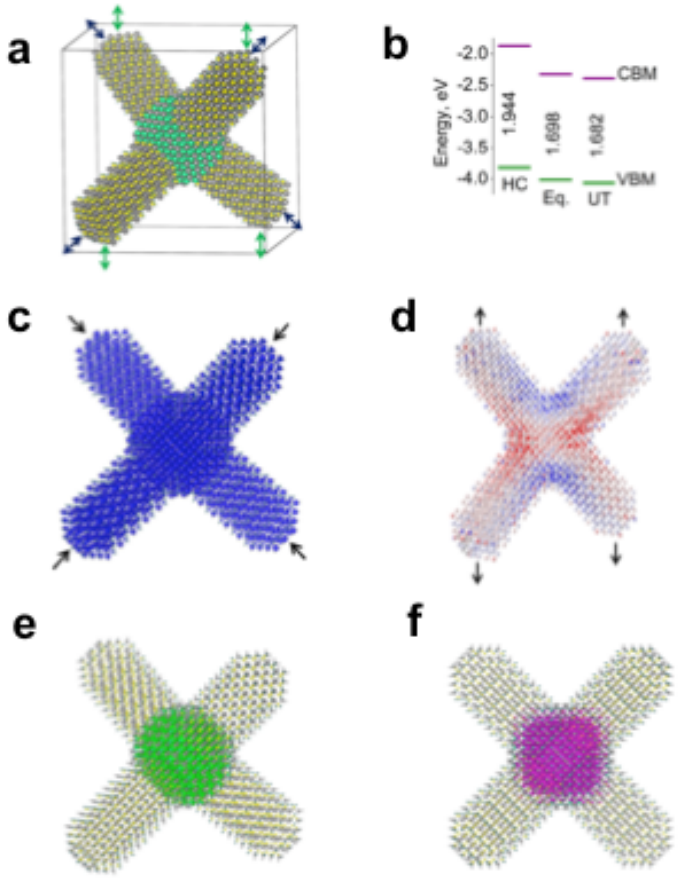

Figure 3.4: Valence force field and density functional calculations of tQD stress response

a. Atomic structure of and schematic of stress application to modeled CdSe/CdS core-arm tQD: zinc-blende CdSe core. b. Energy level changes of stressed tQDs. HC represents energy level changes for a tQD under hydrostatic compression, Eq. represents the energy levels for a tQD at equilibrium (no stress), and UT represents the energy levels for a tQD under uniaxial tension. c-d. Distribution of stresses in tQDs that are c. compressed isotropically and d. stretched uniaxially. Colorbar shows percent change in volume. e-f. Equilibrium (unstressed) wave function charge densities of the valence band maximum and conduction band maximum, respectively.

3.4.2: Micromechanical Finite Element Simulations

To investigate how tQD core compression may arise under overall uniaxial tension of the polymer nanocomposite, we conducted voxel-based micromechanical finite-element analysis simulations of tQDs in a polymer matrix using the Finite Element Analysis Program (FEAP).[99] The simulations used periodic boundary conditions and net average uniaxial loads for a range of packing densities utilizing multiple random configurations to generate valid statistics. As the focus of the analysis was an elucidation of the mechanism leading to net compression of the core, two-dimensional simulations were performed to ease the cost and complexity. Previous comprehensive work considering comparing some nine 2D and 3D unit cells showed only a 5-

10% difference in the results for elastic modulus; since the majority of the blue-shifts and red-shifts that are observed occur in the elastic region, this is further justification for use of a 2D finite element model[100].

Two example configurations are illustrated for low (Fig. 3.5.A) and high (Fig. 3.5.B) tQD aggregate volume fractions, or packing densities. Figure 3.5.C shows the typical pressure response of a CdSe core in the low packing regime; the integral of the pressure field is positive, indicating the overall response is tensile. In contrast, Figure 3.5.D shows a typical pressure response in a CdSe core in the high packing regime; the integral of the pressure field is negative indicating the overall response is compressive. Though it varied significantly depending on the tQD location in the aggregate, the average core stress across all cores and configurations was of similar magnitude for net compressive and net tensile cases. The mechanism leading to the compressive case is one in which the CdS arms strongly interact due to close proximity and have a large span in the direction orthogonal to the loading, *i.e.*, tQDs serve as sensors of nanoscale dispersion, with a dichotomy in response characteristic (*e.g.*, red-shift or blue-shift, or compressive or tensile) depending on whether or not adjacent tQDs are interacting.

By simulating a large ensemble of configurations (~200) we gain a statistical estimate of the probability that a given packing density will lead to a situation in which uniaxial tension gives rise to a net volumetric compression of the CdSe cores in an aggregate. As shown in Fig. 3.5.E, high packing densities lead in a near linear fashion to higher probabilities of net compressive cores over the range of packing densities from ~10 to ~30% (the upper limit of what can be sensibly simulated in two dimensions).

The finite-element analysis reveals a substantial core stress amplification of up to a few orders of magnitude in the tQD for both volumetric compression and tensile stress cases, qualitatively consistent with experimental observations.

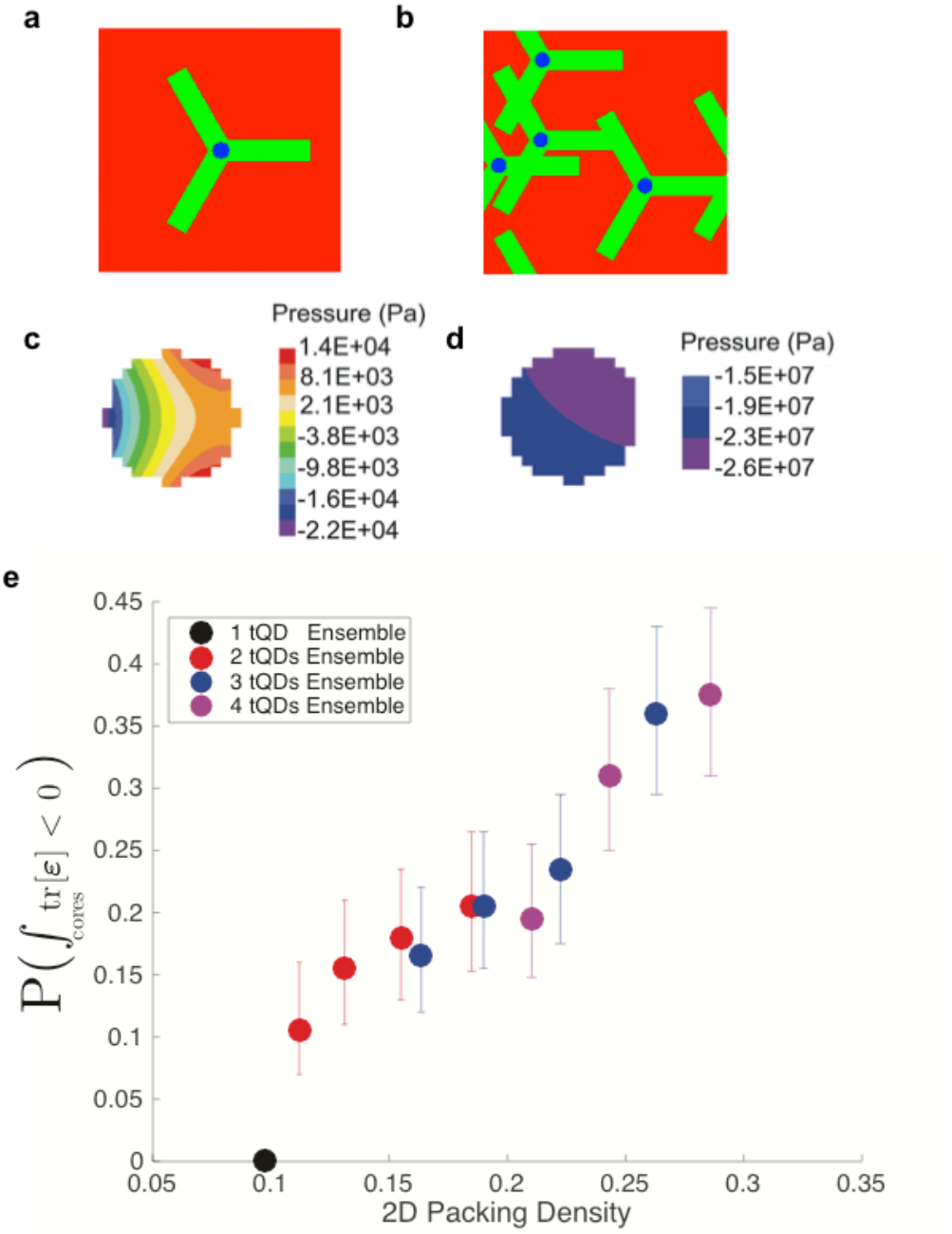
a
b
c
Pressure (Pa)
1.4E+04
8.1E+03
2.1E+03
-3.8E+03
-9.8E+03
-1.6E+04
-2.2E+04
d
Pressure (Pa)
-1.5E+07
-1.9E+07
-2.3E+07
-2.6E+07
e
1 tQD Ensemble
2 tQDs Ensemble
3 tQDs Ensemble
4 tQDs Ensemble
$\mathrm{P}\left(\int_{\mathrm{cores}} \mathrm{tr}[\varepsilon] < 0\right)$
0.45
0.4
0.35
0.3
0.25
0.2
0.15
0.1
0.05
0
0.05
0.1
0.15
0.2
0.25
0.3
0.35
2D Packing Density

Figure 3.5: Finite element analysis of tQD-nanocomposite films
a, b. *Finite element analysis images of low density (tension-sensing) and high density (compression-sensing) tQD aggregate unit cells. In the configurations shown, compression-sensing aggregates have 28% tQDs by area and an applied uniaxial stress of 0.53e+4 Pa, while simulated tension-sensing aggregates have 9.6% tQDs by area and an applied uniaxial stress of 0.14e+4 Pa.* ***c.*** *Pressure map of a tension-sensing tQD core from (a).* ***d.*** *Pressure map of a compression-sensing tQD core from (b).* ***e.*** *Probability that a given tQD configuration at a given tQD volume fraction, or packing density, in an aggregate will result in a net average volumetric compression in the tQD cores. Black, red, blue, and magenta respectively represent ensembles with one, two, three, and four tQDs.*

3.5: Conclusion

In summary, we have presented here a tQD/polymer nanocomposite system produced by low-cost, scalable colloidal processing which can act as a local sensor of tensile or compressive stresses. The stress is measured as shifts in the emission maximum and the full-width half maximum of the photoluminesence spectra, and is readily measurable in structural parts in service using commonly available portable spectrometers and light sources. We show the unique capacity of tQDs to respond to subtle changes in their own nanoscale dispersion and mechanical properties, with a switch in optomechanical response when tQDs are in direct contact. The sensitivity of the responses to deformation is three orders of magnitude greater than for current state-of-the-art tQD sensors and approaches or exceeds existing technologies. Moreover, the inclusion of tQDs in the polymer does not degrade the mechanical properties of the polymer matrix, and there is no reduction in response over >20 cycles of deformation. Simulations show that blue-shifts and red-shifts are due to compression and tension of the tQD core, respectively, during tensile deformation of the entire nanocomposite. The solution-processed tQD merges colloidal synthesis, interfacial tunability, and high sensitivity due to its geometry-borne stress-amplification. The tQD enables facile, scalable introduction into composite materials combined with effective local and bulk sensing capabilities. The tQD's ability to self-detect its own nanoscale dispersion in a composite results in a unique optical nanosensor that can self-report local as well as macroscopic composite properties, a potentially important characteristic for the design of "smart" polymer nanocomposites. Based on the previously established ability of spherical nanoparticles to diffuse to cracks in polymers and diminish their ability to propagate[17], the results in this work could also engender tQD-spherical nanoparticle nanocomposites that could serve as multifunctional, auto-responsive, self-healing, structural parts potentially capable of predicting their own failure in service[17,45].

3.6: Materials and Methods

Methods Summary: CdSe-CdS tQDs were prepared as before[49]. The tQDs had arm length 26 ± 3 nm and diameter 6 ± 0.8 nm. SEBS was provided by Kraton (MD 1537) and dissolved in chloroform (Sigma Aldrich) to create solutions of 150 mg SEBS/~10 mL chloroform for compression-sensing films and 25 mg SEBS/~2 mL chloroform for tension-sensing films. tQDs coated with native hydrophobic ligands were dissolved in chloroform and added to the polymer

solutions at concentrations of 20% by weight/5% by volume of polymer. These precursor solutions were cast into glass petri dishes for compression-sensing films, and allowed to dry under ambient conditions followed by placing under vacuum. The drying process took 5-8 hours. For tension-sensing films, precursor solution was added to a glass vial and subjected to a highly vigorous flow of nitrogen gas resulting in film drying occurring within 1-2 minutes.

The ~75-100 μm thick films were cut into strips 3-20 mm long x 1-3 mm wide for tensile tests, and were clamped using flat grips into a tensile rig employing a Mark-10 0.5 N load-cell. A screw-driven stage connected to a controller (OptoMike OMEC–2BF) was used at a strain rate of 5×10^{-03} sec^{-1}. 19 trials were performed for compression-sensing films, and 13 trials for tension-sensing films. Tests were performed by stretching the sample to a strain of ~0.6 and holding for 28.5 seconds for stress relaxation. To assess repeatability, the same film was cycled >20 times.

To monitor fluorescence while stretching, the rig had a hole for laser passage, and was mounted onto a metal plate for stability. We used an inverted fluorescence microscope with a spectrometer (Acton, SpectraPro-3001) and CCD (Princeton, 7509-0001). Exposure times of 1s were used to collect spectra with 0.6 sec between frames. We used 488-nm Ar+ laser excitation (Lexel Laser, Inc., 95) with 1-W power and 150-μm spot size. We excited/measured photoluminescence from the core due to the type I band alignment, which localizes the electron and hole to the core, and to our 488 nm excitation[49]. Spectra were collected over the laser spot and fit to single Gaussians. Change in emission was defined as the difference between the peak position at time t and at zero strain.

For TEM, sections ~70-90 nm were cut from ~100 um thick films using an RMC MT-X Ultramicrotome (Boeckler) at cryogenic temperature and picked up from water onto copper grids. Staining was performed using RuO_4 to darken PS regions. Stained sections were imaged using a 200 kV Tecnai G220 S-TWIN. Unstained sections were imaged using a 200 kV Tecnai G2. AFM samples were prepared similarly, and were not stained. AFM images were obtained with a scanning probe microscope "NEXT" (NT-MDT) in amplitude modulation mode with a Si probe (spring constant 3.5 N/m). Height and phase images were recorded at the low force level (A_{sp} = 10 nm, A_0 = 12 nm) and high force (A_{sp} = 10 nm, A_0 = 24 nm) level. A_{sp} is set-point amplitude, while A_0 is free oscillation of the probe prior to sample interaction. Contrast in the phase images at low force varies from ~0–10 degrees and in phase images recorded at high force, ~0-80 degrees. We performed quantitative mapping of elastic modulus in Hybrid mode (a non-resonant oscillation mode in which the sample is modulated at 1.5 kHz). This allowed assigning of light-colored phase blocks to PS and darker blocks to softer PEB.

Tomography was performed using an FEI Titan 80-300 TEM operated in high-angle annular dark field STEM mode at 200 kV with a 10-mrad convergence angle. A tilt-series was acquired with 1.5° steps from ±70°, reconstructed using the IMOD software package. To calculate tQD/polymer packing density, the 3D density was filtered with a 3x3x3 3D median filter and thresholded to distinguish tQD from polymer. The polymer/tQD volume ratio was calculated using all voxels within a boundary defined by a convex hull calculation. For average aggregate size and size distribution, a custom image segmentation Matlab algorithm was developed to outline aggregates. >200 aggregates were used to for histograms. The diameter was

computed from a circle with the same area as the aggregate. Compression-sensing aggregates had a diameter of 134±5 nm, while tension-sensing aggregates had a diameter of 292±9 nm. For finding tQD/polymer packing density from TEM images, we estimated the aggregate volume fraction of the polymer from the 2D aggregate fill factor and divided the nanoparticle volume fill fraction by this quantity.

Time-resolved photoluminescence lifetime measurements on compression-sensing and tension-sensing films were performed with a Picoquant FluoTime 300 employing a PMA 175 detector. An LDH-P-C-405 diode laser (excitation wavelength 407.1 nm) was used with a repetition rate of 1 MHz.

Reported errors are standard error of the mean, except for nanoparticle sizes, which are mean and standard deviation.

Detailed Methods for Electronic Structure Calculations: The atomic structure of CdSe/CdS core-shell tQDs was generated using a "nanostructure generator" software package that can generate nanocrystals of arbitrary shape and size. The CdSe core of 2.8 nm has zinc-blende crystal structure; the four CdS arms are of wurtzite crystal structure with dimensions of 4.2 nm in length and 2 nm in diameter. The lattice constants and the internal lattice parameter are taken from bulk experimental measurements[101]. Dangling bonds of the surface atoms are passivated by pseudo-hydrogen atoms, with fractional nucleic and electronic charges, to model an ideal passivation[98]. Overall the system contains 4,245 atoms, which is significantly larger than what direct DFT calculations can perform. Therefore, we employ multilevel divide-and-conquer computations. First, the atomistic valence force field (VFF) method[98] is used to relax the atomic positions. Second, the total charge density of the tQD is generated by assembling of atomic charge motifs using the charge patching method (CPM)[102]. It has been shown that the CPM can yield essentially the same QD charge density as a self-consistent DFT calculation. Third, the total electron potential is generated from the charge density using the PEtot computational package[103]. Fourth, the band-edge eigenstates are solved using the folded spectrum method[104], which allows calculations of the band edge eigenstates with a computational effort that scales linearly with the size of the nanoparticle. The resulting single particle eigenenergies have a typical error of 20 meV compared to direct LDA calculations, and the eigenenergy splittings within valence band and conduction band have typical errors of just 5 meV. Thus the current calculations have almost the same accuracy as direct local density approximation (LDA) calculations. We have used plane-wave basis sets and norm-conserving pseudopotentials with a plane-wave cutoff of 35 Ryd. Spin–orbit interaction is included in the single particle Schrodinger equation. In order to check the applicability of our multilevel computational strategy for deformations, we performed a test using bulk CdSe. The optimized lattice constant for the CdSe zincblende structure using our VFF method is 6.081 Å. Our calculated Poisson's ratio of 0.37 is in agreement with the experimental value[101] of 0.4 and our calculated deformation potential of -3.21 eV is in agreement with the experimental value of -3 eV[104].

The constructed CdSe/CdS core-shell tetrapod has a band gap of 1.698 eV, close to the experimental band gap of 1.9 eV. Valence band maximum (VBM) and conduction band minimum (CBM) are localized in the CdSe core. This core-localization indicates type-I band alignment in the modelled tQD, which is in agreement with previous experimental results[86]. Lower valence band levels (VBM-1, VBM-2, etc) are also localized in the CdSe core, because the 4p(Se)-orbitals have major contribution to CdSe valence band and selenium is less electronegative then sulfur (the sulfur levels are much lower).

Cd-orbitals have a major contribution to the conduction band in both CdSe and CdS bulk structures[57]. Therefore, the conduction band levels in CdSe core and CdS arms are energetically close: core-localized CBM and arm-localized CBM+1 are separated by only 0.185 eV. Moreover, the CdSe core and CdS arms energy levels eventually mix at higher conduction band levels (CBM+4 and CBM+5). The shapes of the conduction band charge densities are similar to previous calculations for CdSe tQDs. Additionally, the CBM partially penetrates in the arms near the core–arm interface.

Since we are applying tensile strain to the polymer, we expect that the tQDs will also experience tensile strain. Therefore, we applied 2.5% tensile strain to the tQD; two of the tQD arms are pulled in one direction while other two arms in the opposite direction. The arm ends are fixed along the deformation axis, while all the other coordinates are relaxed using VFF. The distribution of the local deformation at each atom site (the volume change around each atom) has complex behavior: the deformed tQD shows regions of both tension and compression. Two CdS arms pulled in opposite directions will stretch the region of the CdSe core between them. On the other hand, under tensile strain, the tQD has two pairs of arms that are pulled in the same direction that compress the region of the CdSe core between them like scissors. In case of compressive strain, the situation is the opposite; two arms compress the CdSe core if we push arms in opposite directions and arms pushed in the same strain the joint between them. As a result, a tQD with fixed ends always has regions of both compression and tension simultaneously.

Since the two above described tQD deformations create regions of local tension, the tQD shows a red-shift for both deformations for full VFF relaxation. This is because the region of local tension has the lowest band-gap. At the atomic level, if the distance between two interacting atoms decreases then the gap between their occupied and unoccupied electronic levels increases, if the distance increases the energy gap reduces. The same is applicable to local volumetric deformation around each atom site; local compression increases the energy gap between occupied and unoccupied levels of the atom, while local tension decreases the atomic energy gap. Therefore, when the tetrapod has significant regions of local tension, its band gap decreases (i.e., red-shifts). The calculated band gaps show a small red-shift for the tetrapod under both tension and compression regimes for the case of full VFF relaxation. In addition to the 2.5% uniaxial and hydrostatic distortions, we also examined the effect of tQD structural twisting, which may appear in a polymer matrix under tensile deformation. In cylindrical coordinates, the twisting deformation implies rotation of each atom around the center axis r by an angle $\boldsymbol{\phi}$ varying linearly between -2.5% and 2.5% of a full rotation with respect to the tQD center, such

that $\boldsymbol{\phi}$(i)=(r(i)-r(0))*a, where $\boldsymbol{\phi}$(i) and r(i) are rotation and r coordinate of i-th atom, r(0) radial coordinate of the tQD centre and a=2.352 deg/nm. As with the linear distortions, the ends of the arms are fixed during the VFF relaxation. While the twisting induces regions of compression at the base of the tQD arms in the direction of rotation, it also produces regions under tension between the opposing pairs of arms. The final tQD structure has a small bandgap red-shift of 17 meV.

Chapter 4 : Influence of nanoparticle branching on the Young's modulus of nanocomposites

In previous chapters, we examined key advances in the opto-mechanical sensing ability of tQD-polymer composites. In this chapter, we investigate the improvements in elastic mechanical tunability of these composites as compared to polymer composites of non-branched nanoparticle shapes.

With the availability of nanoparticles with controlled size and shape, there has been renewed interest in the mechanical properties of polymer/nanoparticle blends as nanocomposites. Despite the large number of theoretical studies, the effect of branching for nanofillers tens of nanometer in size on the elastic stiffness of these composite materials has received limited attention. Here, we examine the Young's modulus of nanocomposites based on a common structural block copolymer (BCP) blended with linear nanorods and branched tetrapods, specifically nanoscale tetrapod Quantum Dots (tQDs), in both electrospun fibers and solvent-cast films. We use a phenomenological lattice spring model (LSM) as a guide in understanding the changes in the Young's modulus of such composites as a function of filler shape. Reasonable qualitative agreement is achieved between the LSM and the experimental results for both nanoparticle shapes—with only a few key physical assumptions in both films and fibers—providing insight into the design of new nanocomposites and assisting in the development of a qualitative mechanistic understanding of their properties. The tQDs impart the greatest improvements, enhancing the Young's modulus of SEBS by a factor of 2.5 at 20% loading of tQDs by weight. This is 1.5 times higher than identical composites containing nanorods. An unexpected finding from the simulations is that both the orientation of the nanoscale filler (with respect to the tensile axis) and the orientation of X-type covalent bonds at the nanoparticle-ligand interface are important for optimizing the mechanical properties of the nanocomposites. The branched tQD provides an orientational optimization of the interfacial and filler bonds by a new mechanism not previously recognized as being important for inorganic nanofillers.

4.1: Introduction

Polymer-nanoparticle composites have become a highly active topic of research with rapidly expanding applications[87], in part because of their high polymer-particle interfacial area and the unique shape-and-size dependent, tunable properties of nanoparticle reinforcements. For example, new polymer nanocomposites have been developed which can optically sense stress concentration[18], are responsive to magnetic, electrical, and thermal actuation[105,106], and which exhibit large changes in elastic modulus and glass-transition temperature at low nanoparticle concentrations[107].

While theoretical studies show that the Young's modulus of such polymer nanocomposites depends on nanoparticle shape[108], experimental studies are limited. Experimental studies on polymers[109] include the synergistic reinforcement effects of multiple nanocarbons[110] and the shape-dependent reinforcement effects of micrometer-sized tetrapods[56],

microscale ceramic needles,[64] carbon nanotubes[111], clay-based nanocomposites[112,113], and others[114,115]. Computational studies include the effects of nanoparticle packing and size on the nanocomposite Young's modulus[116,117]. However, the effects of increasing nanoparticle branching on the mechanical behavior of nanocomposites have not been demonstrated[57]. It is possible to make nanocrystals with controlled shapes and degree of branching[53]; as such, they pose an ideal system to study the effect of reinforcement branching.

Here, using nanorods (NRs) and tetrapod quantum dots (tQDs) in both electrospun fibers and solvent-cast films, we studied the effect of increasing nanoparticle branching on the Young's modulus of a common structural elastomer, poly(styrene-block-ethylene-butylene-block-styrene) (SEBS)[118]. We chose SEBS since it is a widely used structural copolymer, has a 40% phase (ethylene-butylene) of similar chemical make-up as our nanoparticle surface ligands (although it is incompatible with 60% of the polymer, the polystyrene phase), and is amorphous, allowing for improved intercalation with the nanoparticles. In choosing polymer-filler nanocomposites, there is a critical choice to be made between the case where the polymer-filler interaction is very strong, in which case the intrinsic polymer structure is disrupted to a high degree, and the case where it is weak, leaving the native polymer structure largely unperturbed. Both limits are of significant interest, but in this first study we focus on the latter weak interface case as it is by far the most common case in practical composites and it is the case which is most amenable to modeling through summation of mechanically independent components. In such a case, the nanoparticles form nanoscopic aggregates distributed throughout the SEBS matrix, due to the van der Waals interactions between the native alkyl ligands on the nanoparticles and the SEBS polymer[11]. No macrophase separation was observed, and no surface modification was performed to achieve single nanofiller dispersion. Future studies will be directed at the single filler dispersed case, where the filler-polymer interaction is much stronger. In the stronger interface case, the nanoparticles may be selectively incorporated within one BCP microdomain and due to their size, the intrinsic local polymer chain conformation may be more affected by the presence of the filler.

In both electrospun fibers and films, we observed nanoscopic aggregates of nanofillers, (~150 nm in diameter), and we found that the multiple-branched tQDs improved the Young's modulus the most compared to linear shapes, *i.e.*, nanoscale branching may optimize the Young's modulus. Our simulated results using a 2D lattice spring model (LSM) suggest that this shape effect on the Young's modulus is primarily due to the orientation of the strong X-type bonds[119] at the nanoparticle-ligand interface. This illustrates the importance of the orientation of both types (filler and interfacial) bonds in increasing the stiffness of structural composites. To the best of our knowledge, our study is the first to examine this effect on the mechanical properties of composites for nanofillers in this size range, thereby providing some new and unique mechanistic insights. We expect that this insight can be exploited to design polymer nanocomposites with optimized mechanical properties for a variety of applications.

4.2: Nanocomposite Preparation and Uniaxial Tensile Testing

The triblock copolymer SEBS (117,000 g/mol molecular weight, 60% polystyrene) with a lamellar microstructure[120] was used as the polymer matrix. CdSe/CdS nanorods (NRs), and CdSe/CdS tQDs were prepared using established methods, and incorporated into the polymer matrix with their native alkyl chain ligands[49]. Polymer nanocomposites were prepared via electrospinning[18] of nanoparticle-polymer solutions in chloroform, while the films were processed by casting of the nanoparticle-polymer solutions into petri dishes. Samples were tested using quasi-static, uniaxial tensile tests to determine the Young's modulus in the small displacement (<0.02 strain) limit. Tests were performed to failure; the average failure strain for fibers was ~100%.

After electrospinning and fiber collection, the mechanical properties of each of the polymer nanocomposites were evaluated using uniaxial tensile tests. Fig. 4.1.A-B show, respectively, the tensile stress-strain curves for electrospun fibers of 20 wt.%/5 vol.% tQD-SEBS nanocomposites, and 20 wt.%/5 vol.% NR nanocomposites. The curves exhibit a high strain and low stress to failure, characteristic of many elastomers. Higher magnification versions of these curves, illustrating the linear elastic regime, are shown in Figs. 4.1.C-D for tQD and NR nanocomposites, respectively.

As can be seen from Fig. 4.1, samples exhibited a processing-inherent variation in moduli and strains at failure of around ~40% covariance for ductility and ~30% covariance for Young's modulus. For tQD and NR-based nanocomposites, the ductility varied minimally with concentration; for the 20 wt.% concentration, the NR composite ductility was 102.8 ± 45.9% and the tQD composite ductility was 102.4 ± 45.5%, similar to the control ductility of 96.0 ± 56.0%. Branched tQDs provide the best performance of any of the fillers, improving the Young's modulus by 2.5 times at 20 wt.% tQD, *i.e.*, a factor of 1.5 times more than linear NRs at the same concentration. The Young's modulus of the unreinforced matrix was 39.7 ±11.8 MPa; for 20 wt.% reinforcement, the modulus of the composites was ~2.5 times higher with tQDs (100.2 ± 28.4 MPa) and ~1.5 times with NRs (66.4 ± 32.1 MPa) for both fibers and films.

4.3: Nanoparticle Dispersion

When the nanoparticles are embedded into the polymer, they partially phase separate, forming aggregates distributed throughout the polymer, as seen in previous studies[18]. This aggregation occurs due to the weak interface between the native alkyl chain ligands on the nanoparticles and the polystyrene (PS) phase of SEBS, which constitutes 60% of the polymer. Though the nanoparticles experience a favorable interaction with the PEB phase of SEBS since they are, as mentioned above, coated with similar alkyl chain ligands, PEB makes up only 40% of the SEBS polymer in this work. The aggregation occurs not due to the favorable interactions with PEB, but to the unfavorable interactions with PS. Fig. 4.2 shows transmission electron microscopy (TEM) images of the NRs and tQDs before (Fig. 4.2.A-B) and after (Fig. 4.2.C-D) integration into polymers. TEM image analysis of over 150 aggregates per sample showed that aggregates formed in the tQD and NR nanocomposites had approximately the same size,

indicating that the nanoparticle aggregate size differences are not responsible for the observed disparities in mechanical properties. As seen in Fig. 4.2.D, tQD aggregates were more porous than the NR aggregates, due to their branched geometry inhibiting close packing, [121,122] evidenced by regions of lighter contrast in tQD aggregates. TEM images show very similar aggregate size and shape between tQDs and NRs. Thus, we attribute our findings on the superior Young's modulus of tQD nanocomposites to nanoparticle shape as opposed to differences in aggregate size on the nanocomposite Young's modulus).

Multiple physical factors including nanoparticle-nanoparticle interactions, polymer-nanoparticle interactions, and variations in electric field in the electrospinning process play critical roles in determining the dispersion of nanoparticles in polymer nanocomposites[57].

In spite of the aggregation observed, there is no degradation in any of the mechanical properties and a shape-dependent enhancement of the Young's modulus for both tQD and NR nanocomposites.

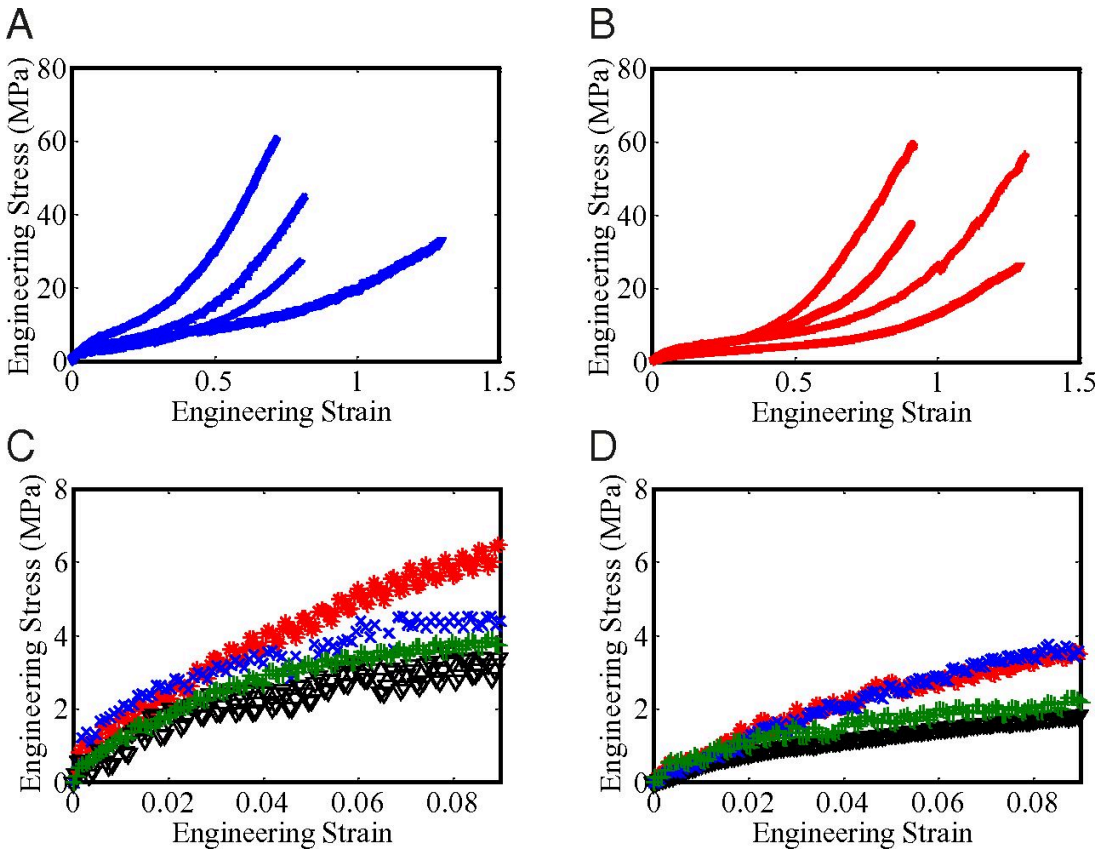

Figure 4.1: Uniaxial tensile stress-strain curves of tQD and NR-nanocomposites
(A) Stress−strain curves of four different 20 wt.% tQD nanocomposite samples. (B) Stress−strain curve of four different 20 wt.% NR nanocomposites. (C) Stress−strain curves of four different 20 wt.% tQD nanocomposites, shown over the first 9% strain to highlight the elastic region occurring from 0 to 2% strain. (D) Stress−strain curves of four different 20 wt.% NR nanocomposites, shown over the first 9% strain to highlight the elastic region.

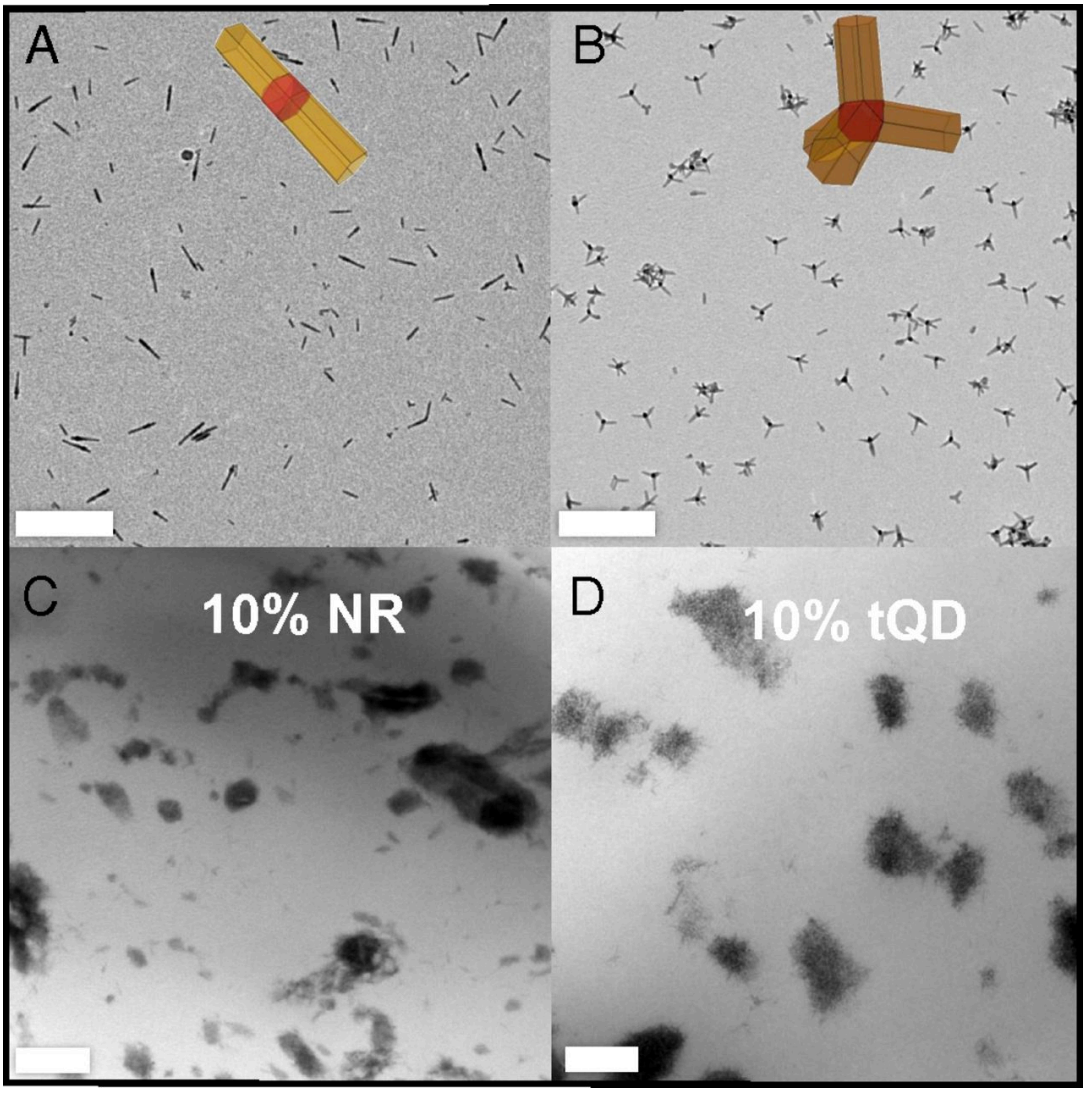

Figure 4.2: Transmission electron micrographs of tQDs, NRs, and their polymer nanocomposites
(A) TEM micrograph of NRs before polymer incorporation. (B) TEM micrograph of tQDs before polymer incorporation. (C) TEM micrograph of NRs after polymer incorporation. (D) TEM micrograph of tQDs after polymer incorporation.

4.4: Simulation of the Young's modulus of tQD- and NR-Nanocomposites

In order to explain these results, we modeled the nanocomposites using elastic LSMs. Elastic LSMs are an alternative to finite element models[123] that model a material as an elastic spring network to estimate the Young's modulus. Elastic LSMs have been shown to reproduce the equations of state for an isotropic elastic medium subjected to small deformations[123]. The LSM used in this work was a two-dimensional model identical in form to the LSM utilized in previous theoretical work on polymer composites[124,125]. Although LSMs which model plastic deformation also exist[124], the LSM used here accounted only for fully elastic deformations[125].

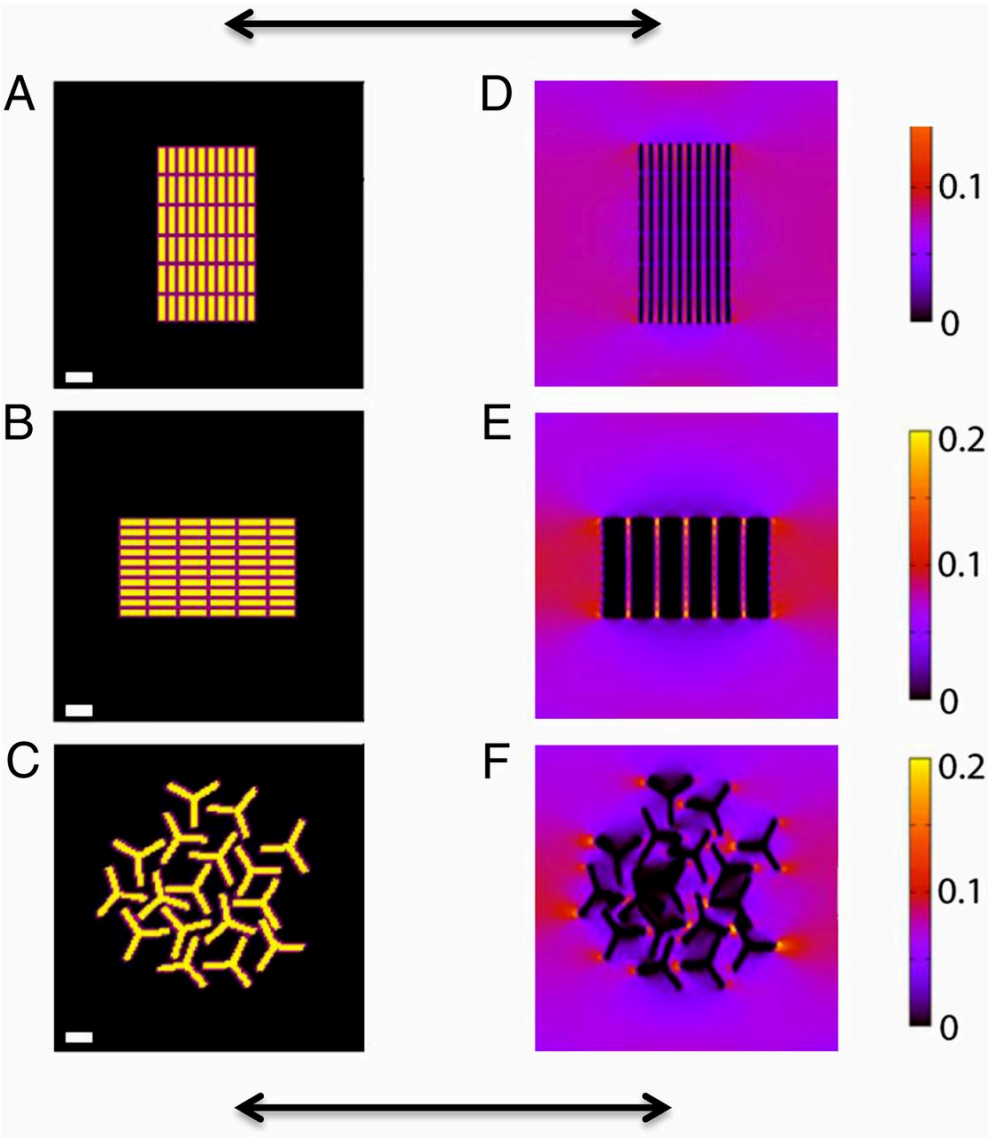

Figure 4.3: Simulations of elastic strain fields in tQD and NR-nanocomposites using a lattice spring model

LSM spring distribution images for (A) vertically aligned NRs, (B) horizontally aligned NRs, and (C) tQDs. (D−F) Corresponding elastic strain fields after stretching. Black double arrows indicate the stretching direction. Scale bars are 25 nm (14 nodes)

Because tQDs form loosely packed assemblies[122] while NRs form closely packed assemblies[121], polymer was included into tQD aggregates in the simulations but not into the NR aggregates. The bond between surface ligands and CdSe/CdS semiconductor nanocrystals is known to be a strong (relative to polymer-polymer interaction) X-type bond[119]. A spring of force constant one thousand times greater than the polymer (and half that of the nanoparticle) was thus situated at the inorganic-organic interface between ligand and polymer.

Using the literature value for the Young's modulus of CdS (E = 90 GPa)[126], and our experimentally measured Young's modulus of SEBS (E = 45 MPa), nanoparticle spring

constants were set to be two thousand times greater than the polymer spring constant. Because the like-like interaction between the nanoparticle ligands and the poly(ethylene-butylene) (PEB) domains is likely weaker than the interactions between the polymer chains, we used ligand/interfacial spring constants that were roughly half the polymer spring constant (this assumption gave the best agreement between theory and experiment)[57]. Once nanoparticles were assigned spring constants and placed in the matrix, the LSM calculated the minimum elastic energy of the spring network under a tensile force, reporting the Young's modulus and Poisson's ratio equilibrium spring configuration under stress.

Fig. 4.3 shows the mask files (before strain application) (Fig. 4.3.A-C) and strain fields (Fig. 4.3.D-F) under uniaxial tension in the simulated micromechanical lattice for the 10 wt.% (2.5 vol.%) NR- and tQD-polymer nanocomposites. Tension was applied to the left and right of the image with equal force. Yellow regions correspond to highest strain, while black regions correspond to regions of zero strain.

As expected, the strain in the nanoparticles is approximately zero due to its 2000 times higher spring constant relative to the polymer matrix. NR or tQD arms aligned with the tensile axis had localized regions of high strain at their apexes (yellow 'hot spots' in Fig. 4.3.E-F). This is likely because regions of low strain are created due to the relative restriction of the polymer matrix along the long axis of an NR or tQD arm. Because of the Poisson effect, regions of high strain are created adjacent to those where the polymer is less restricted, such as at the ends of tQD arms. These yellow 'hot spots' may be good locations for covalent anchoring of the nanoparticles to the polymer to optimize strain transfer and nanocomposite properties[87]. When NRs are orthogonal to the tensile axis, stress transfer is much reduced, resulting in no hot spots of localized strain.

Figure 4.4 shows both the disparity in Young's modulus between tQD-nanocomposites (Fig. 4.4.A) and NR-nanocomposites (Fig. 4.4.B) as well as the reasonable agreement between experimentally obtained and the simulated values for the Young's modulus at different nanoparticle concentrations. For normalization purposes, the Young's modulus of the nanocomposites (E) was divided by the Young's modulus of the pristine polymer (E_0) for all comparison plots. The lines of best fit for experimental and theoretical data match closely (Fig. 4.4.A-B, see Table 1 for details of fit) for all nanoparticle-polymer composites studied. The goodness of fit for the linear fit is slightly better for the NR than the tQD nanocomposites, indicating that tQDs follow a slightly non-linear filler behavior. This is likely due to their branched shape, as explained below. The experimentally observed enhanced filler performance of tQDs, as compared to NRs, is recovered even in a simple two-dimensional LSM, the simplest model we could deploy that shows this effect. We see very good agreement between simulation and experiment for all filler systems studied. Importantly, this good agreement was achieved through a non-arbitrary accounting of only a few key parameters, especially the nanoparticle fill factor and the ratio of polymer to particle stiffness which are known. While the particle-polymer interface spring constant is not independently known, the results of the simulation are only weakly dependent on this quantity as long as it is within a factor of two of the polymer stiffness.

The polymer-nanoparticle interface plays a critical role in the mechanical behavior of the polymer nanocomposites[87]. In fiber composites, little to no mechanical property changes are seen until high volume fractions, partly due to the increased polymer-nanoparticle interface[127]. For all nanocomposites studied here, the greatest difference in the Young's modulus of nanocomposites containing different shapes of nanofiller was seen at the highest concentration, 20 wt.% (5 vol.%). Though the trend is clear, at lower concentrations the experimental scatter is large enough to partially obscure the smaller differences in Young's moduli. Variability in mechanical properties of fibers within a single synthetic batch may be due to inherent sample heterogeneity introduced by the stochastic electrospinning process[128]. Studies have shown that electrospun fibers dry very rapidly as they are drawn through a spatially varying electric field[71], causing them to experience heterogeneous tensile forces and develop highly varying structures[129]. The error bar in the Young's modulus also increased with concentration, likely due to nanoparticle aggregates increasing the heterogeneity of the nanocomposite morphology and acting as nucleation sites for defects.

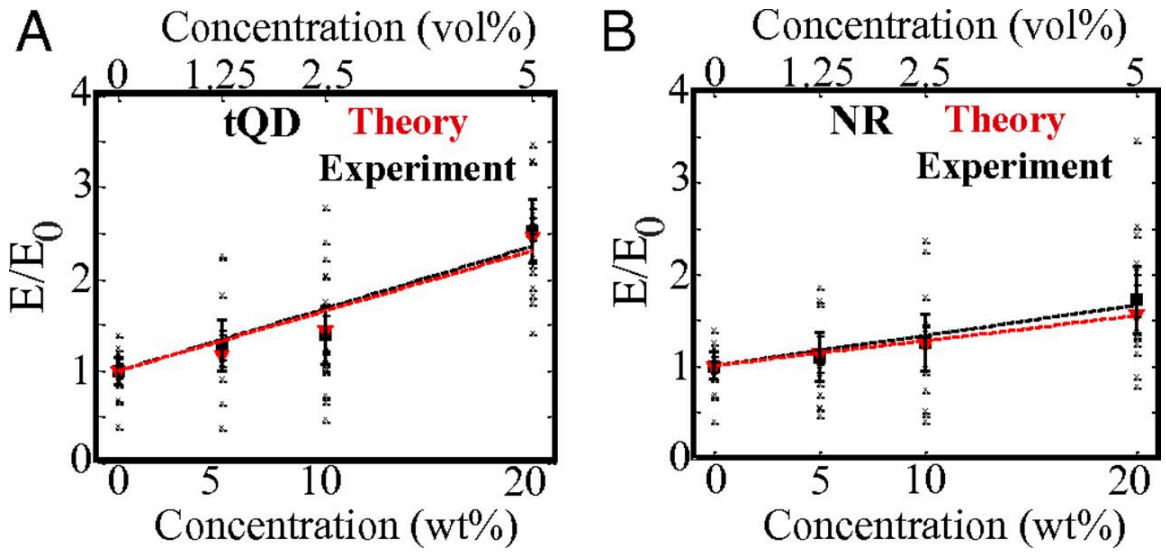

Figure 4.4: Comparison of experimental results with simulated data
Top x axis is volume percent concentration, while bottom x axis is weight percent. (A) Plot of Young's modulus, E, normalized to control modulus, E0, versus nanoparticle concentration for tQD nanocomposites. (B) Plot of Young's modulus, E, normalized to control modulus, E0, versus nanoparticle concentration for NR nanocomposites. Red lines/points represent results from the lattice spring model, while black lines/points represent experimental results. Each black "x" is the result of a single experimental test. Fits are clamped to the (0,1) point, which corresponds to the normalized control modulus.

4.5: Origin of the Disparity between tQDs and NRs: X-Type Interface Orientation

The major finding of this work is that the presence of the tQDs enhanced the Young's modulus of the SEBS polymer to the largest extent, by 2.5 times at 20% loading, more than 1.5 times that of NRs at the same concentration. We discuss four possible explanations for this

phenomenon: i) interface orientation of X-type ligand-nanoparticle bonds, ii) restriction of polymer chains inside porous tQD aggregates, iii) the larger extent of interface in tQDs compared to NR clusters, and iv) additional stress-dissipating bending modes for tQDs due to their branched shape. We conclude, based on our LSM simulations, that optimization of X-type bond interface orientation is a key explanation for the relative enhancement of the Young's modulus of tQD nanocomposites.

One reason for the modulus enhancement can be understood by considering the influence of the filler orientation with respect to the tensile axis. Traditional isostrain and isostress predictions suggest that polymer composites with high aspect ratio ceramic fillers oriented parallel to the tensile axis should be much stiffer than those with fillers orthogonal to the tensile axis[130]. Due to their linear shape[131], the NR aggregates consist of closely packed arrays in which every NR takes the same orientation. Hence, NR nanocomposites consist of NRs that are both parallel and orthogonal to the tensile axis. Due to the more branched, isotropic shape of the tQD, at least one arm is likely to have a component lying along the tensile axis, resulting in a higher Young's modulus on average.

However, the above explanation cannot account for all the effects observed in this study, since the simulated tQD nanocomposites still exhibited a higher elastic modulus than the simulated horizontally oriented NR nanocomposites. A second explanation likely lies in the orientation of the nanoparticle-ligand interface. In the polymer nanocomposites under study here, while the ligand is entangled with the PEB domains of the polymer via relatively weak Van Der Waals forces, as mentioned above there is a much stronger X-type bond between the nanoparticle and its surface ligands[119]. This X-type bond is represented in the LSM by a stiff spring (1000x stiffer than the polymer, and half the stiffness of the nanoparticle spring constant) at the nanoparticle-ligand interface.

We suggest that the orientation of these strong interfacial X-type bonds plays a crucial role in the polymer nanocomposite mechanical behavior (Figure 4.5). NRs perpendicular to the stretching axis have the least filler springs aligned with this axis, and hence have the lowest modulus, in spite of having the most interfacial springs aligned (Figure 4.5.A). While NRs parallel to the tensile axis have the highest number of filler springs (or bonds) aligned with the axis, they also have the least number of interfacial X-type bonds parallel to the axis (Figure 4.5.B) (roughly one aligned interfacial bond for every four un-aligned interfacial bonds, since NRs have a width of 3 nodes and a length of 14 nodes).

Due to their relative isotropy, tQDs have the greatest number of interfacial X-type *and* filler bonds oriented with the axis (Figure 4.5.C) (roughly one aligned bond for every un-aligned bond). The random orientation of both filler and interfacial X-type bonds in tQD composites thus may represent an orientational optimization, enhancing the Young's modulus in tQD nanocomposites. It thus appears that in order to engineer a composite that maximally capitalizes on the strength of both inorganic Cd-S bonds as well as interfacial X-type ligand bonds, it may be highly advantageous to use a multiply branched, isotropic nanofiller such as tQDs.

These results suggest that due to the importance of these bonds for stress transfer to the filler phase, the nanoscale orientation of strong interface bonds with respect to the tensile axis can be an equally important factor in improving the small-displacement elastic mechanical properties of polymer composites as filler bond orientation. The results also suggest that certain branched nanofiller shapes are capable of optimizing the orientations of both key types of bonds to achieve overall optimal stress transfer to the filler phase. This information may be of key importance for engineering nanocomposites with tunable and maximized elastic strength for structural applications.

Another component of this phenomenon is related to the different bending modes accessible to tQDs as opposed to NRs. The branched structure of the tQD may allow it to act as a 'nano-shock absorber' since its arms bend more in response to stress, unlike the rigid, linear NRs. These bending modes conferred by the tQD arms may allow the tQD to dissipate additional stress, possibly contributing to the observed increase in Young's modulus over NR nanocomposites.

In spite of the fact that the polymer-nanoparticle interactions are mainly van de Waals interactions in this study, there are still key differences in mechanical properties of nanocomposites with fillers of different shape. It is our belief that using a weak filler-matrix interfacial interaction is further beneficial so that the variation in the interfacial area among different fillers does not play a critical role.

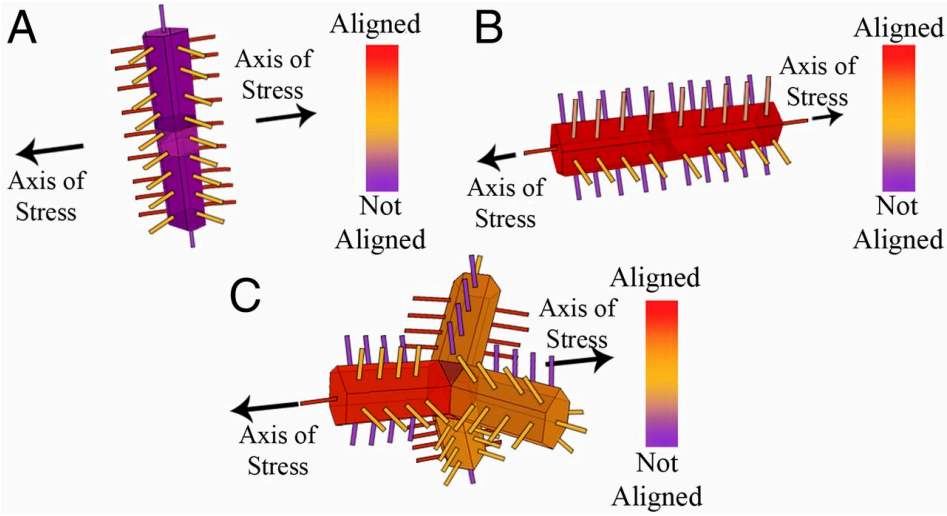

Figure 4.5: Schematic of alignment of nanoparticle springs and X-type interfacial springs in NRs and tQDs with tensile axis
(A) Vertical NRs have some aligned X-type bonds but unaligned filler bonds. (B) Tetrapods have an optimization of aligned filler and interfacial bonds. (C) Horizontal NRs have no aligned interfacial bonds but aligned filler bonds.

4.6: Results on Film Composites

After initial experiments with electrospun fiber matrices, all the experimental results on mechanical testing of composites in this work were reproduced on solvent-cast bulk films of

~100 μm thickness. In the bulk format, the SEBS polymer used in this work is widely employed in everything from sports equipment to electronics. We have found that the nanoparticle dispersion and shape dependence of the Young's modulus for NR- and tQD-based composites roughly matches that of the electrospun fibers within ~10%, with slightly less scatter in the Young's modulus (a factor of ~1.5 less scatter in the raw data) (Figure 4.6). The phase-separated nanoparticle dispersion in these bulk films is roughly similar to that of the electrospun fibers, as shown in Figure 4.7. Since the scatter is only slightly less across 8-9 samples, this suggests that part of the scatter that we see may be due to nanoparticle aggregation, while part may be due to electrospinning structural variations.

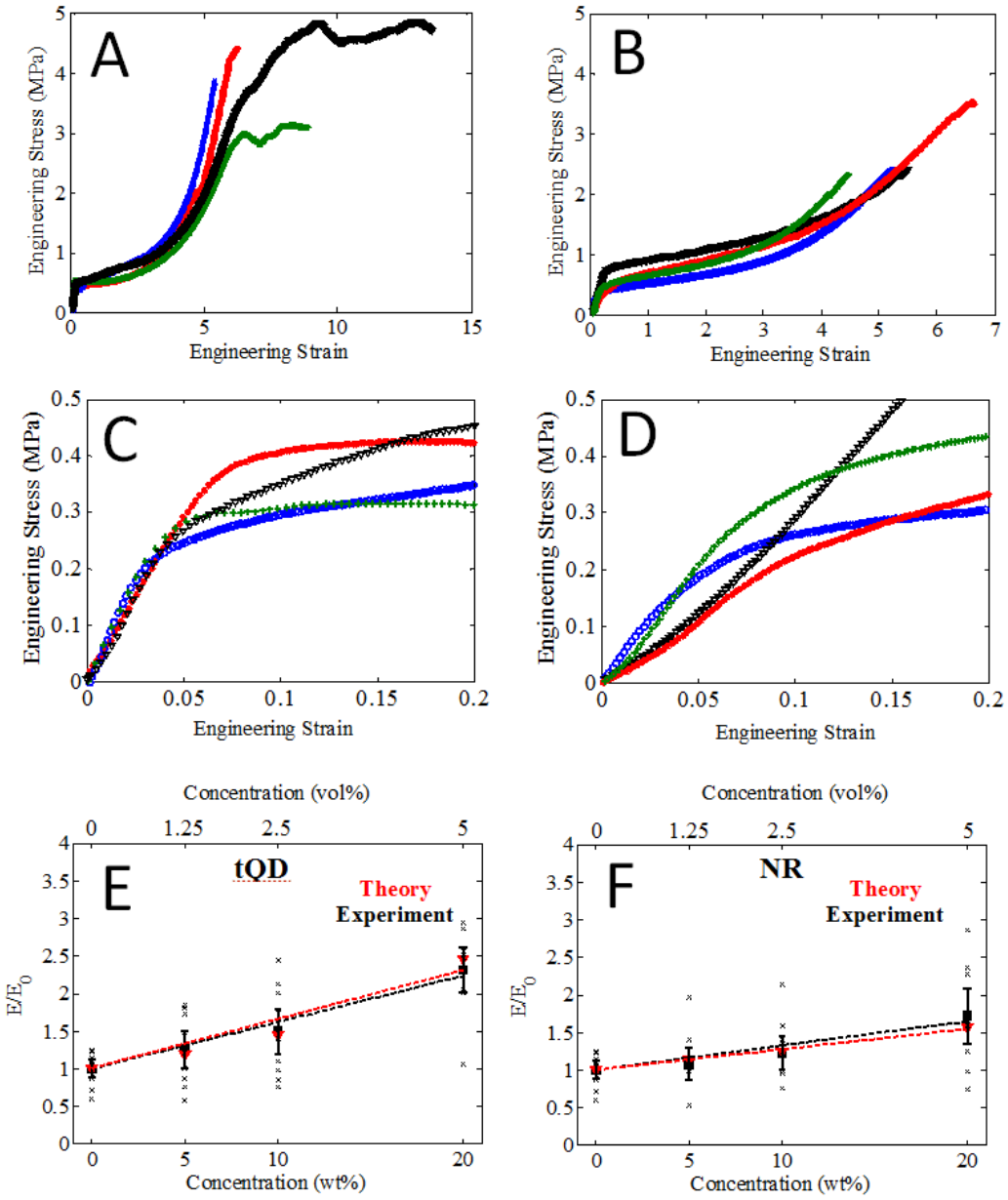

Figure 4.6: Comparison of experimental results on bulk SEBS films with simulated data using lattice-spring model

(A) Example mechanical curves to failure of 20% tQD-SEBS nanocomposite films. (B) Example mechanical curves to failure of 20% NR-SEBS nanocomposite films. (C) Example mechanical curves of 20% tQD-SEBS nanocomposite films, shown over the first 0.2 strain to highlight the elastic region. (D) Example mechanical curves of 20% NR-SEBS nanocomposite films, shown over the first 0.2 strain to highlight the elastic region. Top x-axis is volume percent concentration, while bottom x-axis is weight percent. (E) Plot of Young's modulus (E), normalized to control modulus (E_0) versus nanoparticle concentration for tQD-SEBS film nanocomposites. (F) Plot of Young's modulus (E), normalized to control modulus (E_0) versus nanoparticle concentration for NR-SEBS film nanocomposites. Red lines/points represent results from the lattice-spring model, while black lines/points represent experimental results. Each black "x" is the result of a single experimental test. Linear fits are clamped to the (0,1) point which corresponds to the normalized control modulus.

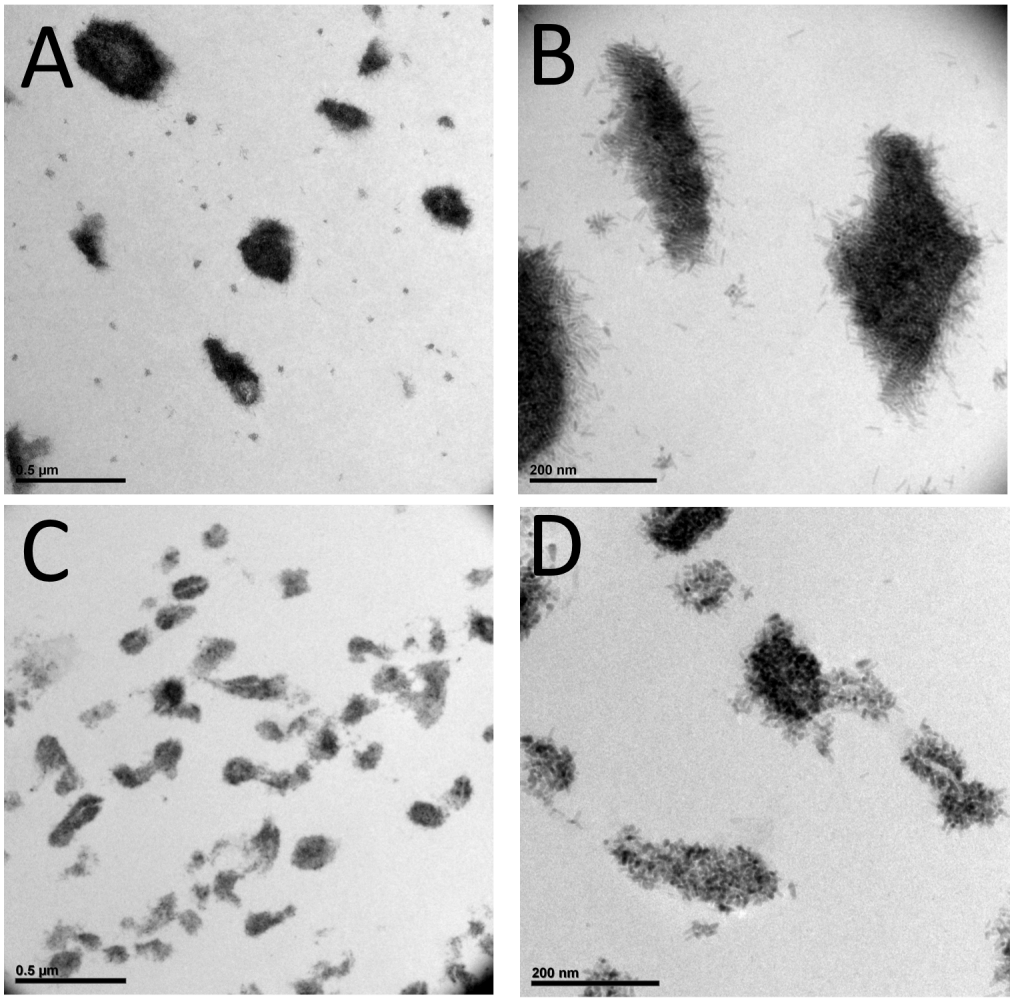

Figure 4.7: Comparison of experimental results on bulk SEBS films with simulated data using lattice-spring model
(A) Wide-area micrograph of 20% NR-SEBS nanocomposites. (B) Close-area micrograph of 20% NR-SEBS nanocomposites. (C) Wide-area micrograph of 20% tQD-SEBS nanocomposites. (D) Close-area micrograph of 20% tQD-SEBS nanocomposites. Scale bars are 500 um (A, C) and 200 um (B, D).

4.7: Simulations of Stiffness as a Function of Aggregate Area Fraction

tQDs and NRs both form similar-sized aggregates with diameters ranging from 2,000-10,000 nm^2, indicating that any difference in Young's modulus between tQDs and NRs is likely due to nanoparticle shape. Simulations of stiffness as a function of aggregate volume fraction (area fraction in 2D) on dipods, rods, and tripods with packing or area fractions ranging from ~20-90% indicate that the stiffness differences are not due to shape effects on aggregate packing. These aggregate area fraction changes result in only 2-6% stiffness changes as compared to ~30-150% across nanoparticle shapes of a given concentration (Figs 4.8-4.9, Table 2). A result of the branched tQD shape is the relative porosity of tQD aggregates seen in the TEM images (Fig. 4.2), leading one to conclude that there is polymer inside of tQD but not NR aggregates[96,122]. Furthermore, the chemical compatibility of the PEB phase of the block copolymer with the nanoparticle surface ligands increases the likelihood that polymer is inside the tQD aggregates. In one hypothesis, the enhanced Young's modulus in tQD composites could be caused by restriction of polymer chains inside these relatively porous tQD aggregates, decreasing local chain mobility. However, again, our simulations indicate that the stiffness of tQD nanocomposites is not dependent on aggregate area fraction or packing density (Figs. 4.8-4.9, Table 2). Experimentally, however, changing nanoparticle packing involves relatively large changes in interface strength[57], so this observation alone is not conclusive. However, restriction of chain mobility in the aggregates in the LSM simulations (by increasing stiffness of the springs inside of the tQD clusters) resulted in arbitrary Young's modulus variations (0-90%) depending on the spring constant of the restricted polymer. Therefore, explanations based on the restriction of polymer chains are not credible as an explanation based on our simulations. The good experimental-theoretical agreement achieved in this work was based on non-arbitrary physical assumptions that did not result in large or random variations with small percent changes.

Thus, although it is likely that polymer is present inside the clusters for enthalpic reasons, we conclude that the restriction of the chains in the cluster may not be a main cause of the relative Young's modulus improvements for our tQD-composites. For entropic reasons, polymer chains tend to favor less ordering, even if enthalpic considerations cause some degree of ordering and restriction. Therefore, it is likely that the polymer chains form a relatively loosely-wrapped interpenetrating network around and inside of the tQD aggregates. A similar analogy is a number of electrical wires which are loosely entangled; while pulling on the wires is easy at first as they slide past one another, it becomes increasingly difficult once a knot is encountered. In the small-displacement elastic limit under study, it is likely that the loosely-wrapped polymer in the tQD aggregate is still in the sliding phase and not yet restricted enough to cause much chain mobility decrease.

Another possible explanation consists of the fact that as tQD clusters have arms protruding out of the cluster and a relatively higher porosity, they have more interface for stress transfer. Furthermore, since the tQD clusters are not densely packed, they should be much softer than those of NRs, with reasonable elasticity to further release the stresses. Indeed, packing rods less densely leads to a slight stiffness increase, leading horizontally aligned NRs to match the stiffness of the relatively isotropic tQDs at loosest packings (Fig. 4.8). However, even very loosely packed rods oriented parallel to the stretching direction do not exceed tQDs in the nanocomposite modulus, implying that based on our simulations this explanation alone cannot explain the discrepancy between tQDs and NRs (Fig. 4.8).

We have conducted simulations, fraction (area fraction in 2D) on the Young's modulus for tQDs, NRs, and dipods, varying the volume fraction (area fraction in 2D) of the aggregate from ~<20-90% at constant nanoparticle fill factor and constant interface width and stiffness. Like tetrapods in 3D, dipods in 2D can approach arbitrarily close, as can interdigitated rods. We found that across the three 2D shapes studied that there was no significant change in the stiffness (only a 2-6% change, (Table 2 and Figs. 4.8-4.9) as compared to 30-150% across shapes at the different concentrations studied). The effect of aggregate area fraction in our 2D lattice spring model is minimal compared to the shape-dependent effects on stiffness. We believe that this is because at the very small displacements below the elastic limit, the polymer trapped in between the tQD aggregates does not get displaced enough for its restricted area to affect the overall stiffness (analogous to electrical cables entangled in a knot, which simply slide before the knot tightens). Table 3 provides a summary of the effect of changing each parameter in the simulations on the resulting normalized stiffness.

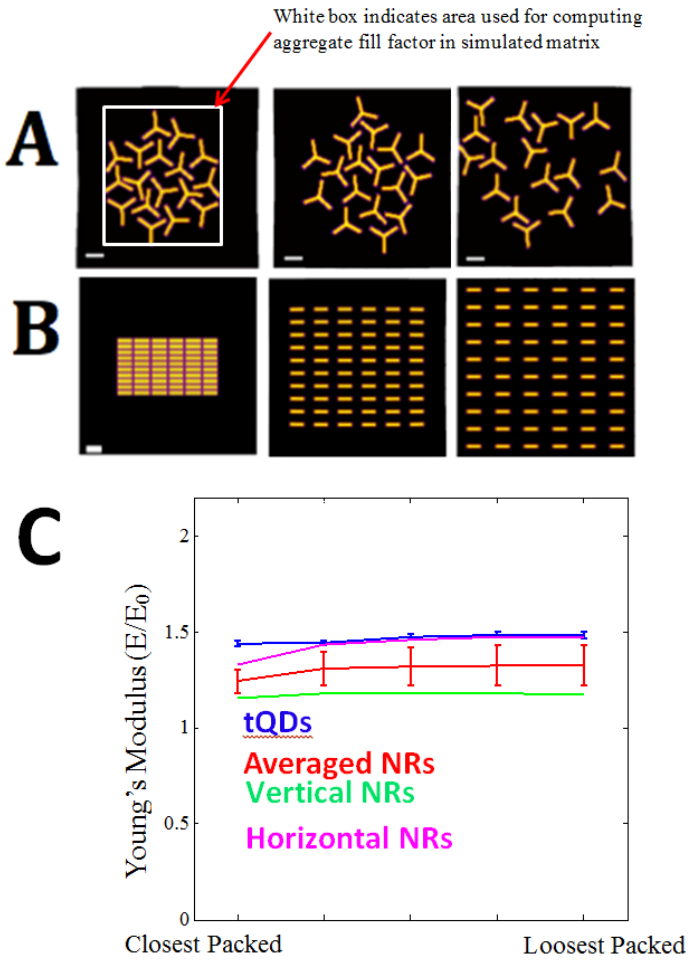

Figure 4.8: Polymer nanocomposite modulus as a function of packing.
(A) Images of tQD aggregates studied with decreasing packing (left to right). The white box indicates the area used in computing the aggregate fill factor. (B) Corresponding image for horizontal NRs. Five total packings were studied. Scale bars are 25 nm for all images, and all images are to the same scale. (C) Plot of Young's modulus (E/E0) vs. packing for NR and tQD nanocomposites. Blue line represents averages of over 12 trials of randomly placed tQDs while the red line represents the average of vertical (green) and horizontal (magenta) NR. All simulations shown in Fig. 4.8 used a nanoparticle area fill factor of 10%, held constant across all stiffness vs. packing simulations. The aggregate fill factor, defined as the area taken up by the entire aggregate, was varied in Fig. 4.8 from 18.5% to 80.5% for NRs and 48.3% to 83.0% for tQDs (closest and loosest packed, respectively; the middle packing was at 51.3% for NRs and 73.2% for tQDs).

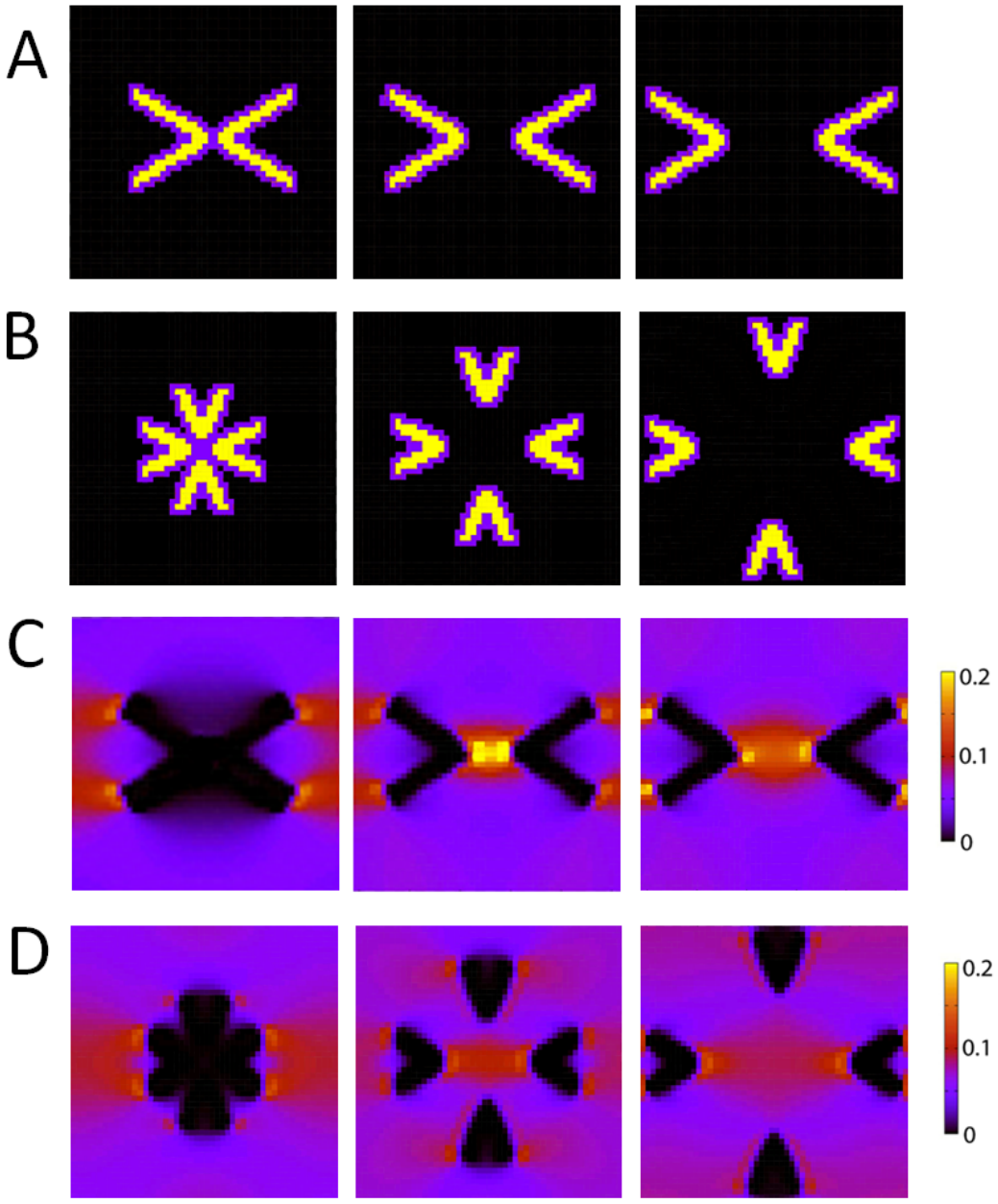

Figure 4.9: Studies of aggregate area fraction occupied by two geometries of dipods on the Young's modulus

A. Mask (input, or spring distribution) files for 2 dipods flipped 180 degrees with respect to each other. B. Mask files for 4 dipods arranged orthogonally. C. Strain distribution images for input files in A. D. Strain distribution images for input files in B. For stiffness changes, see Table 2.

	Parameter	NR fibers	tQD fibers	NR films	tQD films
Experimental Fits	A	0.0330	0.0680	0.0322	0.0617
	B	1.0	1.0	1.0	1.0
Theoretical Fits	A	0.0272	0.0655	0.0272	0.0655
	B	1.0	1.0	1.0	1.0

Table 1: Trendline fits
Slopes (A) and intercepts (B) for the linear fits (fits are clamped to the 0,1 data point) shown in Figs. 4.4 and 4.6. Goodness of fit (R^2) varied between ~0.95 to ~0.99 for NRs and tQDs respectively in both fibers and films.

Packing	Structure (see Fig. 4.9)	Aggregate Area Fill Factor	Nanoparticle Fill Factor	% Change in Stiffness
Closest Aggregate Packing	90 Dipods	24.0%	10%	0%
Intermediate Packing	90 Dipods	52.6%	10%	6.0%
Loosest Packing	90 Dipods	92.3%	10%	6.0%
Closest Packing	180 Dipods	32.8%	10%	0%
Intermediate Packing	180 Dipods	35.6%	10%	4.1%
Loosest Packing	180 Dipods	43.8%	10%	2.7%

Table 2: Stiffness as a function of packing for dipod nanocomposites
The last column of percent changes in stiffness are defined relative to the closest packed composite. The structure '90 dipods' refers to 4 dipods arranged orthogonally, while '180 dipods' refers to 2 dipods as shown in Fig. 4.9.

Importance of Variable for Nanoparticle Type (Y = Important, N = Unimportant/Minimal Effect)	tQDs	NRs	QDs
Placement Angle (in Close-Packed Aggregate)	No	Yes	No
Interfacial Bond Strength	Yes	Yes	Yes
Cavity Shape/Size/Position	N/A	N/A	Yes
Aggregate Packing Density	No	No	No

Table 3: Summary of Effects of Specific Parameters on the Results of the Simulations

4.8: Conclusion

We have studied the effect of branching of nanoparticle fillers on the Young's modulus of polymer nanocomposites. Films and fibers of a common structural block copolymer, SEBS, modified with tQDs of an inorganic filler, increase the Young's modulus significantly more than in composites of linear NRs. Simple 2D lattice-spring model simulations can readily recover this result, and show that the difference in the results mainly from the orientation of the strong X-type bonds at the nanoparticle-ligand interface. Our results suggest that the orientation of strong filler bonds at the inorganic-organic interface between the nanoparticle and polymer is as important of a factor in tuning the Young's modulus as the orientation of nanofiller bonds. The branched tQD, with its relatively isotropic orientation as compared to NRs, optimizes both these orientations to achieve the largest enhancement of the composite Young's modulus. This result may enable design of new nanofillers and nanocomposites of a variety of polymers with optimized mechanical properties. Multiple additional bending modes of the tQD may also contribute to the observed effect by increasing the tQD's ability to dissipate stress over NRs and increasing overall stress transfer to the filler phase.

4.9: Materials and Methods

LSM Simulations of the Polymer Nanocomposites: An alternative to finite element models[123], elastic lattice spring models (LSMs) model a material as an elastic spring network to estimate the Young's modulus. Elastic LSMs have been shown to reproduce the equations of state for an isotropic elastic medium in the case of small deformations[123]. The LSM used in this work was a two-dimensional model identical in form to the LSM in a previous study[124]. Although LSMs which model plastic deformation also exist[124], the LSM used in the present study accounted only for small-displacement (less than ~1%) fully elastic deformations[125].

The data structure for the lattice spring model used in the simulations consists of a simple square lattice (we refer to each lattice point here as a "node") of a network of one-dimensional, Hookean springs connecting nearest and next-nearest neighbors (chosen to be homogeneous to represent the amorphous SEBS matrix in our experimental study[132]). Nano-reinforcements tQDs and NRs had a width of 3 nodes. Each arm of the tQD was 14 nodes long, as was each NR. The nanometer-node equivalency (the number of nodes in the LSM corresponding to nanometers in the nanocomposites) for width was 1.67 nm/node for rods and tetrapods and 0.4 nm/node for dots. For lengths, the ratio was 1.78 nm/node for rods and tetrapods. Changes in nanometer-node equivalencies for lengths between 0.4 to 3 were found to have no impact on results as long as fill factor was kept the same. Furthermore, each particle was surrounded by a one-node wide interface region represented by nodes with a spring constant of 0.5. Tests for NRs and tQDs were all conducted with a constant matrix size of 156x156 nodes, while dipod matrix sizes varied from 48x48 to 52x52 nodes. The matrix size was not found to affect the calculations, though smaller matrices were used to decrease computational times.

In order to properly represent physical conditions, a number of guiding assumptions were made regarding the placement and spring constants of nanoparticles in the lattice spring model. Consistent with previous work[122] as well as transmission electron microscopy (TEM) images of samples in this study (Fig. 4.2), the tetrapod quantum dots (tQDs) were dispersed in porous and loosely packed aggregates. This was anticipated based on previous theoretical studies of nanoparticle superstructure, which indicated that tQDs are likely to remain kinetically arrested in a glassy superstructure due to their multiple arms. Nanorod (NR) aggregates, on the other hand, were closely packed, as demonstrated previously[123]. Each NR was "interdigitated", separated solely by two ligand nodes rather than polymer nodes. Much like tQD nanocomposites, however, simulations revealed that the modulus of NR nanocomposites had little to no dependence on the packing density of the NRs (Fig. 4.8).

Due to the two-dimensional nature of the LSM, area-fill factors obtained from TEM image analysis of our nanocomposites were used for comparison to experimental results rather than using experimental volume fill factors. This was required to achieve good agreement between experiment and theory and is justified by a geometric analysis, which reveals that the 2D and 3D area and volume fill factors differ in two *vs*. three dimensions, with the difference being equal to the ratio of the heights of the polymer and aggregate cylinder. Since these values are unknown, the percentage of nodes assigned as nanoparticle nodes was chosen to identically match the cross-sectional area fill factors (*i.e*., how much of the TEM image was taken up by nanoparticle aggregates) from a TEM image analysis of our nanocomposites (these matched the weight percents (Fig. 4.2)). This is justified by two observations. First, a vast majority of our aggregates (Fig. 4.2) were much larger in size than the microtomed TEM cross-sections (~60 nm), meaning that the images are an accurate 2D representation of our aggregates. Second, due to elongation in the tensile direction during electrospinning, the fibers are approximately cylindrical, meaning that the cross-sectional area fill factor is approximately uniform throughout the fiber length.

After the NPs were placed in the polymer matrix, a tensile stress was applied and the purely elastic strain field corresponding to the lowest energy configuration of the lattice springs was calculated, as well as the Young's modulus and Poisson's ratio. Since the model is deterministic, only one trial was used for each simulation of tetrapods and quantum dots. For rods, two deterministic simulations were performed at each opposing orientation (oriented fully with and against the tensile axis) and the average of these was taken to determine the Young's modulus. Force was applied at the boundary nodes. Spring constants between nodes of different (polymer, nanoparticle, or interface) regions were defined as the average of the different nodes.

The good agreement between experimental results and theoretical LSM predictions was based on non-arbitrary physical assumptions, such as the experimentally-obtained fill factor (from TEM image analysis) and experimentally derived ratios for the nanoparticle and polymer spring constants. The only other variables, the interface spring constant and width, were selected based on experimental ratios for ligand length and nanoparticle size, and the similarity of the ligand shell with poly(ethylene-butylene) (PEB). Changing the value for interface strength did

not lead to significant deviations from experimental values when the interface value was within a factor of two of the polymer spring constant.

Finally we note that purely elastic LSMs, as utilized here and in previous NP-polymer studies,[124] are not perfect models. Since the springs in the LSM are elastic, they are limited in their scope to modeling situations where the displacements are small. Simulation of the nanoparticle-polymer interface comprises an active area of research; the structure of the interface is contested, resulting in uncertainty when simulating the interface. Finally, the conformational entropy of individual polymer chains, which forms the basis for many theories of chain deformation[133], is not accounted for in deriving the elastic energy.

Experimental Materials and Methods: The experimental methods for electrospinning, quantum dot synthesis, electrospinning precursor preparation, tensile testing, and diameter measurements on fibers are the same as in chapter 2 of this thesis. The main difference is that SEBS was employed instead of PLLA as the polymer host matrix, and other key differences are provided herein. Chloroform solutions containing appropriate concentrations of native tQDs or NRs were mixed with premade polymer-chloroform solutions to create solutions of 12% SEBS by weight in chloroform with 5%, 10%, and 20% nanoparticle incorporation by weight of polymer. Solutions were typically made with 25 mg SEBS polymer and about 0.5 mL of chloroform in order to achieve the high viscosity needed for electrospinning. Due to the excellent solubility of the polymer in chloroform, dissolution was observed to occur within minutes. Regardless, solutions were vortexed for several hours to ensure uniformity. Thin film composites of SEBS were prepared by casting mixed solutions of nanoparticles and SEBS in chloroform (~140 mg SEBS in ~8 mL of chloroform) into glass petri dishes and allowing the films to dry in a fume hood before further drying overnight under vacuum. The thickness and width of bulk films (~100 um in thickness, ~1-2 mm in width) were assessed using digital calipers. Uniaxial tensile testing was performed using an Agilent T150 nanomechanical tensile tester. The strain rate was set to 6.9×10^{-3} for all fiber runs and 10×10^{-3} for all film runs, and film strips and fibers glued to tabs were mounted in the tensile tester using standard pivot grips. The average fiber diameter measured over 20-25 samples was around 4 mm ± 1 mm for all nanoparticle shapes tested. The gauge lengths, measured with digital calipers, fell between 6-10 mm for fibers and 1-3 mm for films. No dependence of the Young's modulus on the gauge length was found for either set of samples. For standard tensile mechanical tests, we conducted a total of 14-25 tests per fiber sample of 0%, 5%, 10%, and 20% loading by weight of tetrapods and rods, and 8-9 tests for each film data point. In order to obtain the Young's moduli, linear trendlines were fit to the curve points in the linear elastic region. Data were carefully evaluated to rule out a diameter dependence on mechanical testing. In order to compare mechanical properties between shapes, all aspects of the nanocomposites except nanoparticle shape were kept constant – volume fractions, sample preparation, electrospinning parameters, and mechanical testing parameters such as strain rate.

Chapter 5 : Outlook for the Future

The results of this dissertation highlight the potential of tQDs to serve as stress sensors in structural nanocomposites. However, there are some remaining obstacles to their widespread use in applications in situ, e.g., airframes that have a built-in capability to self-report the development of nanoscale fatigue cracks. These include the inherent toxicity of cadmium and selenium[134,135] and the relatively low deformation potentials of tQDs[89], and the need for detailed, high-resolution three-dimensional mapping around defects to validate tQDs against finite element predictions[136].

Regarding the issue of toxicity, various means to address this problem have been developed[137], include making the tQD out of biologically non-toxic materials, such as zinc oxide[138], coating the tQD with a shell of a less toxic material such as zinc sulfide[139], and wrapping the tQD in biological polymers[140]. While the latter two options are easier places to start, and reduce toxicity for in vitro and in vivo studies of tQDs, they don't solve the problem because cadmium and selenium are still in the nanostructures. Regarding making the tQD out of non-toxic materials like zinc oxide, zinc oxide tetrapod nanocrystals have recently been developed[138]. However, these materials have the issues of being near-UV emitters which require UV rather than visible light sources for excitation, and further tend to have very broad photoluminescence full-width half maxima, which limits their detection resolution and sensitivity.

Further, the tQD stress-sensing pressure coefficient in high-modulus structural polymers is low due to the relatively low pressure coefficients of CdS and CdSe[89]. Future work could consider synthesizing tQDs out of ceramic semiconductor materials with much larger pressure coefficients in order to improve the response sensitivity[141].

Furthermore, a study still remains to be performed in which the optical redshifts during deformation throughout a structural polymer film in which tQDs are well dispersed is mapped in three dimensions. Ideally, this study would be performed using a confocal or near-field microscope in order to achieve diffraction-limited or better resolution. A tQD arm length is typically 30 nm[49], and with a near-field technique such high resolution could be achieved. The results of such high-resolution opto-mechanical mapping, especially around engineered defect shapes representative of classical mechanics solutions, could be compared with the results of finite-element simulations of the same to validate tQDs as an experimental highly local stress-mapping technique[136].

References

(1) Bruns, N.; Pustelny, K.; Bergeron, L. M.; Whitehead, T. A.; Clark, D. S. *Angewandte Chemie* **2009**, *121* (31), 5776–5779.
(2) Gibson, R. F. *Composite Structures* **2010**, *92* (12), 2793–2810.
(3) Noor, A. K.; Venneri, S. L.; Paul, D. B.; Hopkins, M. A. *Computers & Structures* **2000**, *74* (5), 507–519.
(4) Balazs, A. C.; Emrick, T.; Russell, T. P. *Science* **2006**, *314* (5802), 1107–1110.
(5) Breuer, O.; Sundararaj, U. *Polym. Compos.* **2004**, *25* (6), 630–645.
(6) Byrne, M. T.; Gun'ko, Y. K. *Advanced Materials* **2010**, *22* (15), 1672–1688.
(7) Wardle, B. L.; Saito, D. S.; García, E. J.; Hart, A. J.; de Villoria, R. G.; Verploegen, E. A. *Advanced Materials* **2008**, *20* (14), 2707–2714.
(8) Kim, J. S.; Kuk, E.; Yu, K. N.; Kim, J.-H.; Park, S. J.; Lee, H. J.; Kim, S. H.; Park, Y. K.; Park, Y. H.; Hwang, C.-Y.; Kim, Y.-K.; Lee, Y.-S.; Jeong, D. H.; Cho, M.-H. *Nanomedicine: Nanotechnology, Biology and Medicine* **2007**, *3* (1), 95–101.
(9) Smart, S. K.; Cassady, A. I.; Lu, G. Q.; Martin, D. J. *Carbon* **2006**, *44* (6), 1034–1047.
(10) Ciprari, D.; Jacob, K.; Tannenbaum, R. *Macromolecules* **2006**, *39* (19), 6565–6573.
(11) Raja, S. N.; Luong, A. J.; Zhang, W.; Lin, L.; Ritchie, R. O.; Alivisatos, A. P. *Chem. Mater.* **2016**, *28* (8), 2540–2549.
(12) Schadler, L. S.; Giannaris, S. C.; Ajayan, P. M. *Applied Physics Letters* **1998**, *73* (26), 3842.
(13) Velasco-Santos, C.; Martinez-Hernandez, A. L.; Castano, V. M. *Composite Interfaces* **2005**, *11* (8-9), 567–586.
(14) Hanbücken, M.; Müller, P.; Wehrspohn, R. B. *Mechanical Stress on the Nanoscale*; John Wiley & Sons, 2011.
(15) Jarvis, E. A.; Hayes, R. L.; Carter, E. A. *Chemphyschem* **2001**, *2* (1), 55–59.
(16) Li, X.; Chang, W.-C.; Chao, Y. J.; Wang, R.; Chang, M. *Nano Lett.* **2004**, *4*, 613–617.
(17) Gupta, S.; Zhang, Q.; Emrick, T.; Balazs, A. C.; Russell, T. P. *Nature Materials* **2006**, *5* (3), 229–233.
(18) Raja, S. N.; Olson, A. C. K.; Thorkelsson, K.; Luong, A. J.; Hsueh, L.; Chang, G.; Gludovatz, B.; Lin, L.; Xu, T.; Ritchie, R. O.; Alivisatos, A. P. *Nano Lett.* **2013**, *13* (8), 3915–3922.
(19) Kolle, M.; Lethbridge, A.; Kreysing, M.; Baumberg, J. J.; Aizenberg, J.; Vukusic, P. *Advanced Materials* **2013**, *25* (15), 2239–2245.
(20) Choi, C. L.; Koski, K. J.; Olson, A. C. K.; Alivisatos, A. P. *Proceedings of the National Academy of Sciences* **2010**, *107* (50), 21306–21310.
(21) De Wolf, I. *Semicond. Sci. Technol.* **1996**, *11* (2), 139–154.
(22) Sicardy, O.; Touet, I.; Rieutord, F.; Eymery, J. *Journal of Neutron Research* **2001**, *9* (2-4), 263–272.
(23) Vaudin, M. D.; Gerbig, Y. B.; Stranick, S. J.; Cook, R. F. *Applied Physics Letters* **2008**, *93* (19), 193116.
(24) Rabe, U.; Janser, K.; Arnold, W. *Review of Scientific Instruments* **1996**, *67* (9), 3281–3293.
(25) Yamanaka, K.; Nakano, S. *Jpn. J. Appl. Phys.* **1996**, *35* (6S), 3787–3792.
(26) Odegard, G. M.; Gates, T. S.; Herring, H. M. *Experimental Mechanics* **2005**, *45* (2), 130–136.

(27) Liang, X.; Oldenburg, A. L.; Crecea, V.; Chaney, E. J.; Boppart, S. A. *Opt. Express* **2008**, *16* (15), 11052–11065.
(28) Kamat, N. P.; Liao, Z.; Moses, L. E.; Rawson, J.; Therien, M. J.; Dmochowski, I. J.; Hammer, D. A. *Proc Natl Acad Sci U S A* **2011**, *108* (34), 13984–13989.
(29) Jin, X.; Götz, M.; Wille, S.; Mishra, Y. K.; Adelung, R.; Zollfrank, C. *Adv Mater* **2013**, *25* (9), 1342–1347.
(30) Stevenson, A.; Jones, A.; Raghavan, S. *Nano Lett.* **2011**, *11* (8), 3274–3278.
(31) John W Stone; Patrick N Sisco; Edie C Goldsmith; Sarah C Baxter, A.; Catherine J Murphy. *Nano Lett.* **2006**, *7* (1), 116–119.
(32) Pan, L.; Chortos, A.; Yu, G.; Wang, Y.; Isaacson, S.; Allen, R.; Shi, Y.; Dauskardt, R.; Bao, Z. *Nat Comms* **2014**, *5*, 3002–3002.
(33) Lee, C. K.; Davis, D. A.; White, S. R.; Moore, J. S.; Sottos, N. R.; Braun, P. V. *J. Am. Chem. Soc.* **2010**, *132* (45), 16107–16111.
(34) Han, X.; Liu, Y.; Yin, Y. *Nano Lett.* **2014**, *14* (5), 2466–2470.
(35) Zhao, Q.; Wood, J. R.; Wagner, H. D. *Applied Physics Letters* **2001**, *78* (12), 1748.
(36) O'Shea, S. J. *J. Vac. Sci. Technol. B* **1996**, *14* (2), 1383.
(37) Fitzpatrick, M. E.; Lodini, A. *Analysis of Residual Stress by Diffraction using Neutron and Synchrotron Radiation*; CRC Press, 2003.
(38) Dagdeviren, C.; Shi, Y.; Joe, P.; Ghaffari, R.; Balooch, G.; Usgaonkar, K.; Gur, O.; Tran, P. L.; Crosby, J. R.; Meyer, M.; Su, Y.; Webb, R. C.; Tedesco, A. S.; Slepian, M. J.; Huang, Y.; Rogers, J. A. *Nat Mater* **2015**, *14* (7), 728–736.
(39) Mikos, A. G.; Sarakinos, G.; Leite, S. M.; Vacanti, J. P.; Langer, R. *Biomaterials* **1993**, *14* (5), 323–330.
(40) Levental, I.; Georges, P. C.; Janmey, P. A. *Soft Matter* **2007**, *3* (3), 299–306.
(41) Suresh, S. *Acta Materialia* **2007**, *55* (12), 3989–4014.
(42) Talapin, D. V.; Lee, J.-S.; Kovalenko, M. V.; Shevchenko, E. V. *Chem. Rev.* **2010**, *110* (1), 389–458.
(43) Choi, C. L.; Alivisatos, A. P. *Annu. Rev. Phys. Chem.* **2010**, *61* (1), 369–389.
(44) Raja, S. N.; Olson, A. C. K.; Limaye, A.; Thorkelsson, K.; Luong, A.; Lin, L.; Ritchie, R. O.; Xu, T.; Alivisatos, A. P. *Proc Natl Acad Sci U S A* **2015**, *112* (21), 6533–6538.
(45) Wu, D. Y.; Meure, S.; Solomon, D. *Progress in Polymer Science* **2008**, *33* (5), 479–522.
(46) Fiore, A.; Mastria, R.; Lupo, M. G.; Lanzani, G.; Giannini, C.; Carlino, E.; Morello, G.; De Giorgi, M.; Li, Y.; Cingolani, R.; Manna, L. *J. Am. Chem. Soc.* **2009**, *131* (6), 2274–2282.
(47) Reiss, P.; Protière, M.; Li, L. *Small* **2009**, *5* (2), 154–168.
(48) Huang, J.; Kovalenko, von, M.; Talapin, von, D.; Kovalenko, M. V.; Talapin, D. V. **2010**, 1–3.
(49) Talapin, D. V.; Nelson, J. H.; Shevchenko, E. V.; Aloni, S.; Sadtler, B.; Alivisatos, A. P. *Nano Lett.* **2007**, *7* (10), 2951–2959.
(50) Fiore, A.; Mastria, R.; Lupo, M. G.; Lanzani, G.; Giannini, C.; Carlino, E.; Morello, G.; De Giorgi, M.; Li, Y.; Cingolani, R.; Manna, L. *J. Am. Chem. Soc.* **2009**, *131* (6), 2274–2282.
(51) Schrier, J.; Lee, B.; Wang, L.-W. *J. Nanosci. Nanotech.* **2008**, *8* (4), 1994–1998.
(52) Fang, L.; Park, J. Y.; Cui, Y.; Alivisatos, P.; Shcrier, J.; Lee, B.; Wang, L.-W.; Salmeron, M. *The Journal of Chemical Physics* **2007**, *127* (18), 184704.

(53) Manna, L.; Milliron, D. J.; Meisel, A.; Scher, E. C.; Alivisatos, A. P. *Nat Mater* **2003**, *2* (6), 382–385.
(54) Choi, C. L.; Koski, K. J.; Sivasankar, S.; Alivisatos, A. P. *Nano Lett.* **2009**, *9* (10), 3544–3549.
(55) Raja, S. N.; Zherebetskyy, D.; Wu, S.; Ercius, P.; Powers, A.; Olson, A. C. K.; Du, D. X.; Lin, L.; Govindjee, S.; Wang, L.-W.; Xu, T.; Alivisatos, A. P.; Ritchie, R. O. *Nano Lett.* **2016**, acs.nanolett.6b01907.
(56) Jin, X.; Deng, M.; Kaps, S.; Zhu, X.; Hölken, I.; Mess, K.; Adelung, R.; Mishra, Y. K. *PLoS ONE* **2014**, *9* (9), e106991.
(57) Bockstaller, M.; Mickiewicz, R.; Thomas, E. *Advanced Materials* **2005**, *17* (11), 1331–1349.
(58) Mordehai, D.; Kazakevich, M.; Srolovitz, D. J.; Rabkin, E. *Acta Materialia* **2011**, *59* (6), 2309–2321.
(59) Yarin, A. L.; Koombhongse, S.; Reneker, D. H. *J. Appl. Phys.* **2001**, *90* (9), 4836–4846.
(60) Medintz, I. L.; Uyeda, H. T.; Goldman, E. R.; Mattoussi, H. *Nat Mater* **2005**, *4* (6), 435–446.
(61) Greiner, A.; Wendorff, J. H. *Angew. Chem. Int. Ed.* **2007**, *46* (30), 5670–5703.
(62) Li, D.; Wang, Y.; Xia, Y. *Nano Lett.* **2003**, *3* (8), 1167–1171.
(63) Park, J.-S. *Advances in Natural Sciences: Nanoscience and Nanotechnology* **2010**, *1* (4), 1–6.
(64) Peng, F.; Shaw, M. T.; Olson, J. R.; Wei, M. *J. Phys. Chem. C* **2011**, *115* (32), 15743–15751.
(65) Reneker, D. H.; Yarin, A. L.; Fong, H.; Koombhongse, S. *J. Appl. Phys.* **2000**, *87* (9), 4531–4547.
(66) Reneker, D. H.; Yarin, A. L. *Polymer* **2008**, *49* (10), 2387–2425.
(67) Behler, K. D.; Stravato, A.; Mochalin, V.; Korneva, G.; Yushin, G.; Gogotsi, Y. *ACS Nano* **2009**, *3* (2), 363–369.
(68) Ko, F.; Gogotsi, Y.; Ali, A.; Naguib, N.; Ye, H.; Yang, G. L.; Li, C.; Willis, P. *Advanced Materials* **2003**, *15* (14), 1161–1165.
(69) d'Almeida, J. R. M.; Monteiro, S. N.; Menezes, G. W.; Rodriguez, R. J. S. *Journal of Reinforced Plastics and Composites* **2007**, *26* (3), 321–330.
(70) Jin, S. H.; Park, Y.-B.; Yoon, K. H. *Composites Science and Technology* **2007**, *67* (15-16), 3434–3441.
(71) Wu, X.-F.; Salkovskiy, Y.; Dzenis, Y. A. *Applied Physics Letters* **2011**, *98* (22), 223108.
(72) Callister, W. D.; Rethwisch, D. G. *Fundamentals of Materials Science and Engineering*; John Wiley & Sons, 2012.
(73) Takagi, H.; Ichihara, Y. *JSME International Journal Series A* **2004**, *47* (4), 551–555.
(74) Monette, L.; Anderson, M. P.; Ling, S.; Grest, G. S. *J Mater Sci* **1992**, *27* (16), 4393–4405.
(75) Rezgui, F.; Swistek, M.; Hiver, J. M.; G'Sell, C.; Sadoun, T. *Polymer* **2005**, *46* (18), 7370–7385.
(76) Narmoneva, D. A. *Journal of Biomechanical Engineering* **2002**, *124* (2), 223–228.
(77) Mathur, V.; Dixit, M.; Rathore, K. S.; Saxena, N. S.; Sharma, K. B. *Front. Chem. Sci. Eng.* **2010**, *5* (2), 258–263.

(78) Webster, T. J. T. *International Journal of Nanomedicine* **2010**, 299.
(79) Marom, G.; Fischer, S.; Tuler, F. R.; Wagner, H. D. *J Mater Sci* **1978**, *13* (7), 1419–1426.
(80) Voigt, W. *Lehrbuch der Kristallphysik Teubner, Leipzig 1910; reprinted (1928) with an additional appendix*; Leipzig, 1966.
(81) Reuss, A. *ZAMM - Zeitschrift für Angewandte Mathematik und Mechanik* **1929**, *9* (1), 49–58.
(82) Tobolsky, A. V. *J. Appl. Phys.* **1956**, *27* (7), 673–685.
(83) Schrier, J.; Lee, B.; Wang, L.-W. *J. Nanosci. Nanotech.* **2008**, *8* (4), 1994–1998.
(84) Tolls, V.; Aziz, M. J.; Raja, S. *Bulletin of the American Astronomical Society* **2009**, *41*, 346.
(85) Raja, S. N.; Aziz, M. J.; Foley, J. W.; Tolls, V. SPIE, 2009; Vol. 7440, p 744018.
(86) Choi, C. L.; Li, H.; Olson, A. C. K.; Jain, P. K.; Sivasankar, S.; Alivisatos, A. P. *Nano Lett.* **2011**, *11* (6), 2358–2362.
(87) Balazs, A. C.; Emrick, T.; Russell, T. P. *Science* **2006**, *314* (5802), 1107–1110.
(88) Shan, W.; Walukiewicz, W.; Ager, J. W.; Yu, K. M.; Wu, J.; Haller, E. E. *Applied Physics Letters* **2004**, *84* (1), 67.
(89) Li, J.; Wang, L.-W. *Applied Physics Letters* **2004**, *85* (14), 2929.
(90) Roberts, D. R. T.; Holder, S. J. *Journal of Materials Chemistry* **2011**, *21* (23), 8256.
(91) Bao, S.; Li, J.; Lee, K. I.; Shao, S.; Hao, J.; Fei, B.; Xin, J. H. *ACS Appl. Mater. Interfaces* **2013**, *5* (11), 4625–4631.
(92) Crooker, S. A.; Hollingsworth, J. A.; Tretiak, S.; Klimov, V. I. *Phys. Rev. Lett.* **2002**, *89* (18), 186802–186802.
(93) Lunz, M.; Bradley, A. L.; Chen, W.-Y.; Gerard, V. A.; Byrne, S. J.; Gun'ko, Y. K.; Lesnyak, V.; Gaponik, N. *Phys. Rev. B* **2010**, *81* (20), 205316.
(94) Hiemenz, P. C.; Lodge, T. P. *Polymer Chemistry, Second Edition*; CRC Press, 2007.
(95) Kim, J. Y.; Raja, S.; Stellacci, F. *Small* **2011**, *7* (17), 2526–2532.
(96) Tam, E.; Podsiadlo, P.; Shevchenko, E.; Ogletree, D. F.; Delplancke-Ogletree, M.-P.; Ashby, P. D. *Nano Lett.* **2010**, *10* (7), 2363–2367.
(97) Ye, X.; Zhu, C.; Ercius, P.; Raja, S. N.; He, B.; Jones, M. R.; Hauwiller, M. R.; Liu, Y.; Xu, T.; Alivisatos, A. P. *Nat Comms* **2015**, *6*, 10052.
(98) Pryor, C.; Kim, J.; Wang, L. W.; Williamson, A. J.; Zunger, A. *J. Appl. Phys.* **1998**, *83* (5), 2548.
(99) Taylor, R. L. *University of California at Berkeley* **2005**.
(100) Böhm, H. J.; Han, W. *Modelling Simul. Mater. Sci. Eng.* **2001**, *9* (2), 47–65.
(101) Likos, C. N.; Löwen, H.; Watzlawek, M.; Abbas, B.; Jucknischke, O.; Allgaier, J.; Richter, D. *Phys. Rev. Lett.* **1998**, *80* (2), 4450–4453.
(102) Wang, L.-W. *Annu. Rev. Phys. Chem.* **2010**, *61* (1), 19–39.
(103) Chen, F.; Gerion, D. *Nano Lett.* **2004**, *4* (10), 1827–1832.
(104) Wang; Zunger, A. *J. Phys. Chem. B* **1998**, *102* (34), 6449–6454.
(105) Lendlein, A.; Kelch, S. *Angewandte Chemie International ...* **2002**.
(106) Wanasekara, N. D.; Stone, D. A.; Wnek, G. E.; Korley, L. T. J. *Macromolecules* **2012**, *45* (22), 9092–9099.
(107) Ramanathan, T.; Abdala, A. A.; Stankovich, S.; Dikin, D. A.; Herrera-Alonso, M.; Piner, R. D.; Adamson, D. H.; Schniepp, H. C.; Chen, X.; Ruoff, R. S.; Nguyen, S. T.; Aksay, I. A.; Prud'Homme, R. K.; Brinson, L. C. *Nature Nanotech* **2008**, *3* (6), 327–

331.
(108) Knauert, S. T.; Douglas, J. F.; Starr, F. W. *Journal of Polymer Science Part B: Polymer Physics* **2007**, *45* (14), 1882–1897.
(109) Tjong, S. C. *Materials Science and Engineering: R: Reports* **2006**, *53* (3-4), 73–197.
(110) Prasad, K. E.; Das, B.; Maitra, U.; Ramamurty, U.; Rao, C. N. R. *Proceedings of the National Academy of Sciences* **2009**, *106* (32), 13186–13189.
(111) Coleman, J. N.; Khan, U.; Blau, W. J.; Gun'ko, Y. K. *Carbon* **2006**, *44* (9), 1624–1652.
(112) Lan, T.; Pinnavaia, T. J. *Chem. Mater.* **1994**, *6* (12), 2216–2219.
(113) Kojima, Y.; Usuki, A.; Kawasumi, M.; Okada, A.; Fukushima, Y.; Kurauchi, T.; Kamigaito, O. *J. Mater. Res.* **1993**, *8* (5), 1185–1189.
(114) Bernardi, M.; Raja, S. N.; Lim, S. K. *Nanotechnology* **2010**, *21* (28), 285607.
(115) Siqueira, G.; Bras, J.; Dufresne, A. *Biomacromolecules* **2008**, *10* (2), 425–432.
(116) Shou, Z.; Buxton, G. A.; Balazs, A. C. *Composite Interfaces* **2003**, *10* (4-5), 343–368.
(117) Buxton, G. A.; Balazs, A. C. *Molecular Simulation* **2004**, *30* (4), 249–257.
(118) Raja, S. N.; Basu, S.; Limaye, A. M.; Anderson, T. J.; Hyland, C. M.; Lin, L.; Alivisatos, A. P.; Ritchie, R. O. *Materials Today Communications* **2015**, *2*, e33–e37.
(119) Owen, J. S.; Park, J.; Trudeau, P.-E.; Alivisatos, A. P. *J. Am. Chem. Soc.* **2008**, *130* (37), 12279–12281.
(120) Seguela, R.; Prud'Homme, J. *Macromolecules* **1981**, *14*, 197–202.
(121) Kim, F.; Kwan, S.; Akana, J.; Yang, P. *J. Am. Chem. Soc.* **2001**, *123* (18), 4360–4361.
(122) Blaak, R.; Mulder, B. M.; Frenkel, D. *The Journal of Chemical Physics* **2004**.
(123) Ostoja-Starzewski, M. *Appl. Mech. Rev.* **2002**, *55* (1), 35–60.
(124) Buxton, G. A.; Care, C. M.; Cleaver, D. J. *Modelling Simul. Mater. Sci. Eng.* **2001**, *9* (6), 485–497.
(125) Buxton, G. A.; Balazs, A. C. *The Journal of Chemical Physics* **2002**, *117* (16), 7649–7658.
(126) Madelung, O.; Osten, von der, W.; Rössler, U. *Intrinsic Properties of Group IV Elements and III-V, II-VI and I-VII Compounds / Intrinsische Eigenschaften Von Elementen Der IV. Gruppe und Von III-V-, II-VI- und I-VII-Verbindungen*; Springer Science & Business Media, 1986.
(127) Joseph, P. V.; Joseph, K.; Thomas, S. *Composites Science and Technology* **1999**.
(128) Bognitzki, M.; Czado, W.; Frese, T.; Schaper, A.; Hellwig, M.; Steinhart, M.; Greiner, A.; Wendorff, J. H. *Advanced Materials* **2001**, *13* (1), 70–72.
(129) Qiao, B.; Ding, X.; Hou, X.; Wu, S. *Journal of Nanomaterials* **2011**, *2011* (9), 6–7.
(130) Kim, H. S. *Materials Science and Engineering: A* **2000**, *289* (1-2), 30–33.
(131) Baker, J. L.; Toney, M. F.; Geissler, P. L.; Alivisatos, A. P.; Widmer-Cooper, A. **2009**.
(132) Sierra, C. A.; Galan, C.; Fatou, J. G.; Parellada, M. D.; Barrio, J. A. *Polymer* **1997**, *38* (17), 4325–4335.
(133) Buxton, G.; Balazs, A. *Phys. Rev. E* **2003**, *67* (3), 031802.
(134) Winnik, F. M.; Maysinger, D. *Accounts of Chemical Research* **2013**, *46* (3), 672–680.
(135) Hardman, R. *Environmental Health Perspectives* **2006**, *114* (2), 165–172.
(136) Matthews, F. L.; Davies, G. A. O.; Hitchings, D.; Soutis, C. *Finite Element Modelling of Composite Materials and Structures*; Elsevier, 2000.
(137) Bradburne, C. E.; Delehanty, J. B.; Boeneman Gemmill, K.; Mei, B. C.; Mattoussi, H.; Susumu, K.; Blanco-Canosa, J. B.; Dawson, P. E.; Medintz, I. L. *Bioconjugate Chem.*

2013, *24* (9), 1570–1583.
(138) Modi, G. *Adv. Nat. Sci: Nanosci. Nanotechnol.* **2015**, *6* (3), 033002.
(139) Pilla, V.; Alves, L. P.; Iwazaki, A. N.; Andrade, A. A. *Applied Spectroscopy* **2013**, *67* (9), 997–1002.
(140) Shen, L. *Journal of Functional Biomaterials* **2011**, *2* (4), 1–18.
(141) Wei, S.-H.; Zunger, A. *Physical Review B* **1999**, *60* (8), 5404–5411.